Evaluation of nonlinear dynamic phenomena in the hysteretic behaviour of magnetorheological dampers

DOI:
10.1016/j.apples.2020.100019

Document Version
Final published version

Applications in Engineering Science 3 (2020) 100019

Contents lists available at ScienceDirect

Applications in Engineering Science

journal homepage: www.elsevier.com/locate/apples

Evaluation of nonlinear dynamic phenomena in the hysteretic behaviour of magnetorheological dampers

Wael Elsaady[a,b,*], S Olutunde Oyadiji[a], Adel Nasser[a]

[a] Department of Mechanical, Aerospace and Civil Engineering, Faculty of Science and Engineering, The University of Manchester, M13 9PL Manchester, UK
[b] Mechanical Engineering Branch, Military Technical College, Cairo 11838, Egypt

ARTICLE INFO

Keywords:
MR fluids
MR dampers
Finite element analysis
Finite volume analysis
Computational fluid dynamics
Rheology

ABSTRACT

The performance of a commercially-available magnetorheological (MR) damper is modelled via a one-way coupled numerical viscoelastic–viscoplastic approach. The approach adopts a Finite Element Analysis (FEA) of the magnetic circuit of the damper and a transient Computational Fluid Dynamics (CFD) analysis of fluid flow. The apparent viscosity of the MR fluid is defined as a function of the magnetic field intensity and local shear rate. The effects of different sources of the hysteretic behaviour of MR dampers, namely: fluid compressibility, fluid inertia, viscoelasticity and friction are investigated. Moreover, the effect of employing different rheological models in the numerical approach is investigated. The results indicate that that the effects of fluid compressibility and dynamic friction are the main sources of the hysteretic behaviour of the damper. Also, the results show the proper selection of the rheological model employed in the numerical approach is critical, as it leads to major differences in the predictions of the numerical approach.

1. Introduction

Magnetorheological (MR) dampers are a class of semi-active smart devices that manifest highly nonlinear behaviours due to the interactions between multi-physics phenomena that combine structural mechanics, magnetism and rheological fluid flow (Goldasz, 2019). MR dampers are employed in different mechanical systems such as luxury cars, buildings, bridges and railway systems, prosthesis, and aircraft mechanisms (Ahmadian and Norris, 2008; Ahamed et al., 2018; Yuan et al., 2019; Dominguez et al., 2008).

Modelling of the rheological flow in MR fluid applications is thought to be complicated, as it involves interactions between magnetic and dynamic flow characteristics that are affected by different sources of nonlinearity, such as magnetic saturation, non-Newtonian viscoelastic-viscoplastic flow, temperature, fluid inertia, and compressibility (Gurubasavaraju et al., 2018; Guo et al., 2019; Guo and Xie, 2019). The rheological flow is affected by the magnetic field, which is not homogenous in the whole fluid domain in the damper. Rather, it is localised in the throttling area of the damper. This inhomogeneity of the distribution of magnetic field brings an additional difficulty in the definition of the characteristics of rheological flow in modelling approaches (Kemerli et al., 2018; Elsaady et al., 2020). Therefore, most of the existing models of MR dampers in the literature adopt analytical models and solutions that do not depend on modelling of that rheological flow. Rather, most of these models depend on damper representation by a set of springs, dashpots, and other elements that represent nonlinearity (Wang and Liao, 2011). Studies on the numerical modelling of MR fluid devices are uncommon compared to those that employ analytical methods (Goldasz, 2019; Elsaady et al., 2020).

Regarding numerical modelling approaches, Parlak et al. (2012) presented a numerical approach for modelling the viscoplastic fluid flow in MR dampers. Gurubasavaraju et al. (2018) employed a similar technique for the same purpose. Both techniques employed a Finite Element (FE) model for the solution of magnetic field in conjunction with a Computational Fluid Dynamics (CFD) model that investigates the characteristics of rheological flow. In those two papers, the effect of the magnetic field was only defined at the locations of magnetic poles that impose a uniform magnetic field. However, the effect of the non-uniform distribution of the magnetic field along the throttling area of the damper was recently considered in Kemerli et al. (2019), in which the enhanced model shows a better accuracy relative to the experimental data.

Case et al. (2014) developed a two-way coupled approach for a small-scale MR damper used in an orthotics system. For a large-scale MR damper, Zheng et al. (2014) used a two-way coupled technique in which they included the effects of fluid temperature. The flow of MR fluid in these studies was assumed as incompressible viscoplastic flow. Therefore, the models were shown to be incapable of representing the hysteretic behaviours of the dampers, which is mainly caused by the effects

* Corresponding author at: Department of Mechanical, Aerospace and Civil Engineering, Faculty of Science and Engineering, The University of Manchester, M13 9PL Manchester, UK.
E-mail addresses: wael.abdelmoneamelsaady@manchester.ac.uk, wael.elsaady@mtc.edu.eg (W. Elsaady).

https://doi.org/10.1016/j.apples.2020.100019
Received 17 June 2020; Received in revised form 23 September 2020; Accepted 24 September 2020
Available online 30 September 2020

of fluid compressibility, friction, inertia, viscoelasticity, and presence of a gas chamber in common designs of MR dampers (Gołdasz et al., 2018; Syrakos et al., 2018). Recently, an FE approach has been presented in Guo et al. (2019) and Guo and Xie (2019), in which the compressibility and inertial effects were modelled and found to be mainly responsible for the hysteretic behaviours of the dampers. However, not many studies investigated other sources of nonlinearity such as the viscoelastic effects, presence of gas pocket, friction, and other sources of inertia.

Unlike common analytical models of MR dampers, this paper presents a one-way coupled numerical viscoelastic-viscoplastic approach for the analysis of a commercially-available MR damper. The results of the numerical approach have been validated by experimental measurements. The paper aims to model and evaluate the different phenomena that are reported to cause the hysteretic behaviour of MR dampers such as fluid compressibility, inertia, friction and viscoelasticity by using the numerical approach. In most studies that employ numerical techniques, the effect of viscoelasticity and fluid compressibility are neglected (Ahamed et al., 2018; Gurubasavaraju et al., 2018a, 2018b; Parlak et al., 2012;Case et al., 2013, 2014; Bulea et al., 2012; Parlak and Engin, 2012), whereas the current study accounts for these effects. Besides, it accounts for the other sources of nonlinearity caused by the presence of gas pocket in the damper and inertial effects of fluid due to piston motion with higher velocity. Moreover, the numerical approach has been used to evaluate the hysteretic behaviour of MR dampers due to dynamic friction force.

The paper is organised as follows: the construction and experimental characterisation of the MR damper under investigation in this study are presented in Section 2. Then, the method of the numerical viscoelastic-viscoplastic approach and the coupling technique are illustrated in Section 3, followed by the validation of the model and the study of the effects of the variation of different parameters in Section 4. Afterwards, the effect of dynamic friction caused by the sealing glands of the damper is evaluated using the current theoretical and experimental methods, as shown in Section 5. Finally, the conclusions are drawn in Section 6.

2. Construction and experimental characterisation of the MR damper

The MR damper under investigation in this study is the short-stroke MR damper, model RD-8040-1, produced by LORD Corporation. It is a mono-tube MR damper with an air chamber appended to the damper to work as an accumulator. The chamber contains air under certain pressure, and is separated from the fluid domain by means of a diaphragm. The gas pre-charge pressure is required to reduce the effects of cavitation (Lord Corporation, 2019a). The construction and main dimensions of the damper are presented in (Seid et al., 2018; Purandare et al., 2019), and also shown in Fig. 1. The piston provides the housing for an electromagnetic coil that generates the magnetic field in the piston, as shown in Fig. 1(b).

The dynamic characteristics of the damper were measured by the Electro-Servo-Hydraulic (ESH) machine, which applies sinusoidal excitations to one end of the damper and measures the output force on the other blocked end. Therefore, the kinetics of the damper in terms of force, velocity and displacement were determined at different excitation currents applied to the damper, as shown in Fig. 2. It is seen that the output force of the damper increases significantly with the increase of input current. While the piston is operated at 1 A, which is the maximum operating current of the damper according to the damper datasheet (Lord Corporation, 2019b), the maximum force of the damper was found to be approximately 20 times greater than the off-state force of the damper. The current experimental data were found to match those measured for the same damper in Desai et al. (2019), and they were used to validate the mathematical approach presented in the current study.

It is worth mentioning that the measurements of the dynamic characteristics of the damper shown in Fig. 2 do not include the static force of the damper caused by the pre-charge pressure in the air chamber. The damper was installed on the ESH test machine so that the piston was initially fixed at a certain level at which the force monitored by the ESH machine was set as zero. Therefore, the force measured by the ESH machine is the dynamic force of the damper. That is why the force diagrams shown in Fig. 2 are seen to be nearly symmetric about the x-axis, unlike those presented in Lord Corporation, 2019b and Sapiński et al. (2020) in which the force diagrams are seen to be asymmetric about the x-axis. That is because the force diagrams measured in these studies (Lord Corporation, 2019b; Sapiński et al., 2020) represent the total force of the damper which includes the static force due to the pre-charge pressure in the gas chamber. The sole contribution of gas pressure in the current measurements is due to the variation of gas pressure caused by the motion of the piston. That variation is due to the change of volume caused by the immersed/protruded part of the piston rod. Therefore, the output force of the damper according to the current measurements can be expressed as follows:

$$F = p_{reb}\left(A_p - A_r\right) - p_{com}A_p - \Delta F_{gas} - f\left(v_p/\left|v_p\right|\right) \tag{1}$$

where A_p and A_r are the cross-sectional areas of the piston head and piston rod, respectively, p_{reb} and p_{com} are the pressures in the rebound and the compression chambers, respectively, ΔF_{gas} is the variation of gas pressure due to the change of air volume caused by the piston motion, and $f\ (v_p/|v_p|)$ is the summation of all friction resistances multiplied by the velocity sign to interpret its direction as a resisting force.

Eq. (1) has been used to validate the current numerical approach by the determination of different parameters via the numerical approach, and the direct comparison between the theoretical results and experimental data, as will be shown in Section 4.2. The current numerical approach accounts for the pressure and viscous forces, and the friction force caused by the shear stresses on piston walls caused by the flow MR fluid, denoted as the "wet friction" (Chen, 2014; Cantelli, 2009), as will be shown in Section 3.3. The "dry" friction force caused by the gland sealing applied to the piston was neglected. However, the current numerical approach has been used to evaluate the dry friction, as will be shown in Section 5. The variation of the gas force, ΔF_{gas}, is determined assuming adiabatic expansion of gas according to the following equation (Seid et al., 2018):

$$\Delta F_{gas} = p_o A_p \left[\left(\frac{V_{ai}}{V_{ai} + x_p A_r}\right)^m - 1\right] \tag{2}$$

where p_o is the pre-charge pressure of the air chamber whose value is approximately 3.44 bar, based on some data provided to the first author from Lord Corporation, 2019a. V_{ai} is the initial volume of the gas (nitrogen) chamber, x_p is the piston displacement, and m is the polytropic exponent of nitrogen taken as 1.4.

3. Mathematical approach

The current method adopts the same numerical approach presented by the current authors in Elsaady et al. (2020), in which a one-way coupled numerical approach was developed to model the performance of MR dampers. The numerical method couples an FE model developed for the magnetic circuit and a transient numerical model of fluid flow that is implemented using a CFD model. The coupling between the two solvers was implemented by the definition of fluid viscosity as a function of the magnetic field density and local shear rate, as in Kemerli et al. (2018, 2019) and Elsaady et al. (2020). Different numerical modelling approaches that employ either decoupled or one- or two-way coupled techniques between the magnetic field and fluid flow solvers in MR fluid research have been recently reviewed in Elsaady et al. (2020).

The former study, Elsaady et al. (2020) presented a theoretical study of the viscoplastic flow in an MR damper that was previously-tested in Chooi (2005) and Chooi and Oyadiji (2009). The approach presented in the current study expands the former approach by the inclusion of the viscoelastic–viscoplastic behaviour of the fluid. Moreover, the current study shows the roles of compressibility, viscoelasticity, fluid inertia

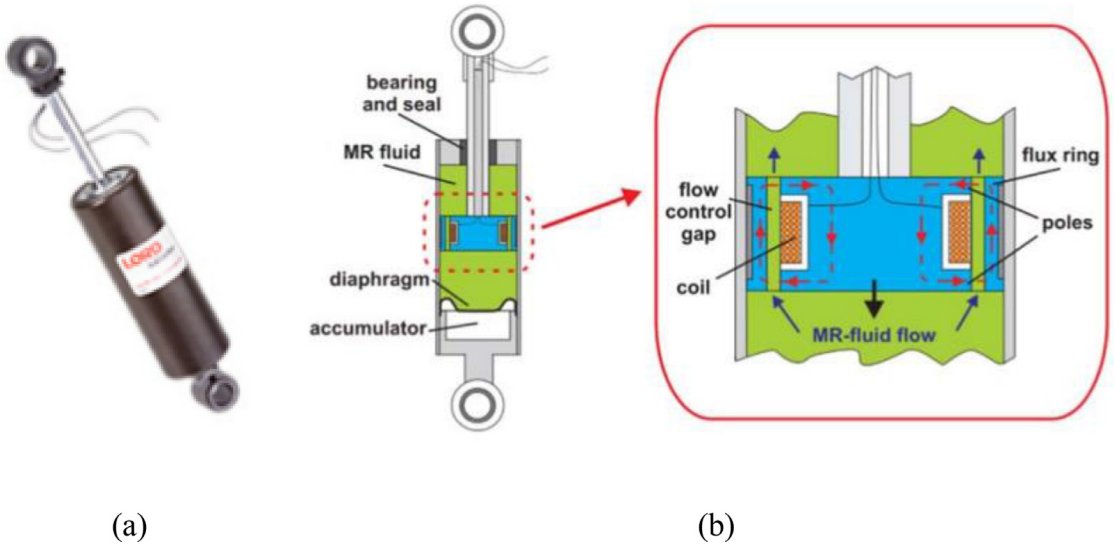

Fig. 1. Construction of the RD-8040-1 MR damper: (a) pictorial view (Ahamed et al., 2018), and (b) schematic cross-sectional view (Purandare et al., 2019).

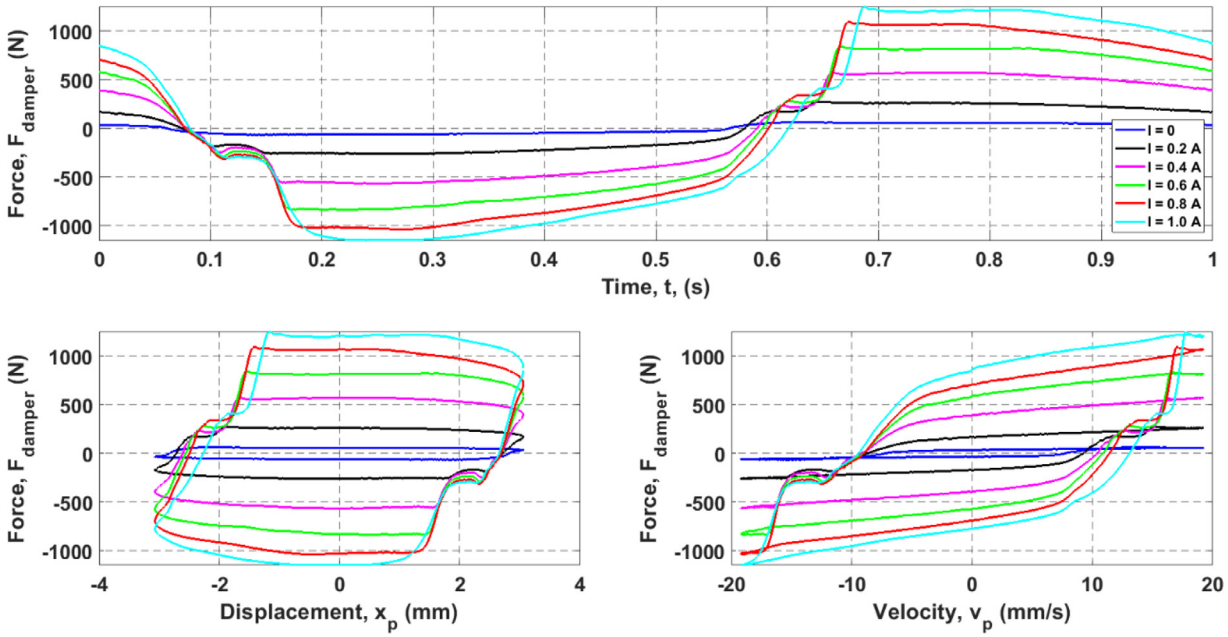

Fig. 2. Dynamic characteristics of the RD-8040-1 MR damper: (up) force–time histories in a complete cycle at different currents, $f = 1$ (Hz), $x_{amp} = 3$ (mm), (down-left) Force–displacement diagrams, and (down-right) force–velocity diagrams.

and friction in producing the hysteretic behaviour of a commercially-available MR damper. The motion conditions of the damper involve very high shear rates of the fluid compared to those conditions studied in Elsaady et al. (2020). That is because the thickness of the throttling area of the current damper is smaller than that considered in Elsaady et al. (2020). Therefore, the rheological model used in the current study is different from the one presented in Elsaady et al. (2020). Also, the effects of magnetic saturation and fluid inertia are included in the current study, whereas they are not presented in Elsaady et al. (2020). The dynamic characteristics measured for the current MR damper were compared with the theoretical results predicted by the numerical approach.

3.1. Generation of computational domains and model conditions

The FE analysis of the electromagnetic circuit is performed using COMSOL/Multiphysics software, whereas the fluid flow analysis is applied by ANSYS/Fluent software. The CFD model is a two-phase flow analysis based on the Volume-of-Fluid (VOF) model in ANSYS/Fluent, to account for the existence of the air chamber in the damper. The computational domains of both solvers are shown in Fig.3(a) and (b), respectively. Fig. 3(a) shows a two-dimensional axisymmetric grid established by COMSOL/Multiphysics for the magnetic circuit of the MR damper (piston head), in which magnetic insulation was assumed at the boundaries of the piston. The mesh is refined in the MR fluid region, as shown in the figure to determine the magnetic field distribution accurately. The direction of current in the coil and the number of coil turns are defined in the FE model based on Maxwell's equations. Also, the nonlinear magnetic properties due to magnetic saturation are accounted for in the model by the definition of magnetic permeability of materials according to the corresponding $B - H$ curve.

Fig. 3(b) shows the fluid domain of the damper described by a two-dimensional axisymmetric grid that is solved in ANSYS/Fluent using

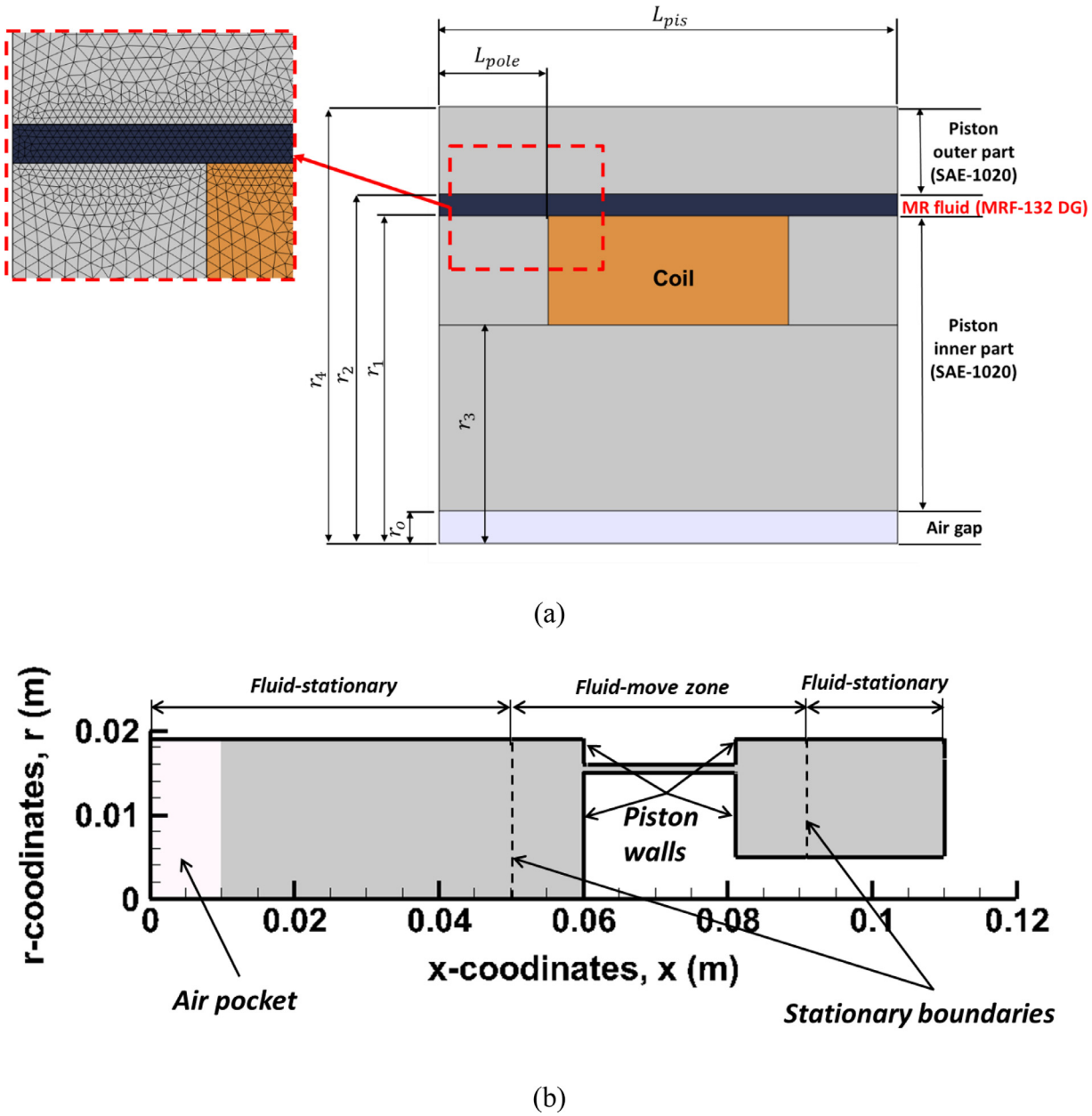

Fig. 3. Computational domains of the current numerical approach: (a) the magnetic circuit domain established for the piston using COMSOL/Multiphysics, and (b) the two-phase flow fluid domain solved by ANSYS/Fluent.

a transient two-phase flow model. All boundaries are defined as walls except for the axis of symmetry. The fluid is excited by the motion of piston walls causing it to flow in the throttling area of the piston. To simulate piston motion in the model, the dynamic mesh layering technique available in ANSYS/Fluent was used. Dynamic mesh layering technique adds or removes cells adjacent to moving walls or fluid zones in a computational domain that can be only represented by quadrilateral cell shapes for 2D problems, or wedge and hexahedron cell shapes for 3D problems (Ansys, 2009). A predefined velocity was assigned to a part of the computational domain, termed as "fluid-movement zone". To do so, two stationary interior boundaries were assigned so that the layering (adding or removing cells from the mesh) is performed.

The dynamic layering technique adopted to simulate the piston movement can be performed by another method, which seems to be more straightforward. That is to assign the motion to the walls of the piston rather than assigning a "fluid-movement zone" and two stationary interior boundaries, as shown in Fig. 4 and also presented in Elsaady et al. (2019). In that case, there is no need to assign the stationary interior boundaries shown in Fig. 3(b) because the moving piston walls perform the layering on the stationary mesh. However, this approach is not employed in the current study, as it is thought to be problematic in terms of solution setup and stability. The problems arise from the need to assign "interface" boundary conditions perpendicular to the moving walls if the motion is assigned to walls rather than fluid zones. This means that at least two interfaces should be defined in the way shown in Fig. 4, which will cause ANSYS/Fluent to read the mesh as three separate meshes split by the two interfaces. This may lead to convergence problems that can be imagined as fluid separation at the interfaces. Therefore, interfaces

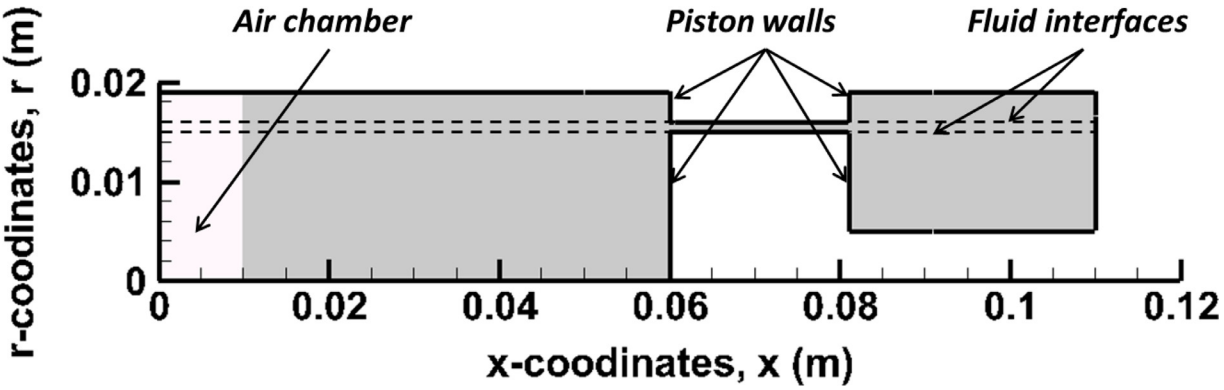

Fig. 4. Mesh interfaces required to assign the motion to solid walls rather than a fluid zone (not applied in the current study).

Table 1
Values of the rheological parameters of Susan-Resiga (2009) and the bi-viscous Bingham model (Ellam et al., 2006).

Susan-Resiga model				Bi-viscous Bingham model	
	$I = 0.2$ A	$I = 0.4$ A	$I = 1.0$ A		$I = 0.2$ A
η_o (Pa.s)	84×10^5	55.78×10^5	55.78×10^5	μ_s (Pa.s)	1420
$\dot{\gamma}^*$ (s^{-1})	7.556×10^{-5}	2.673×10^{-4}	2.673×10^{-4}	μ_p (Pa.s)	3
τ_1 (Pa)	258.7	757.5	1100	$\dot{\gamma}_k$ (s^{-1})	2
n	0.855	0.855	0.855		

are not recommended in CFD simulations if they do not represent the real problem description such as an interface between two rigid bodies.

3.2. Coupling technique

A User-Defined Function (UDF) performs the coupling between the FE and CFD models by the definition of fluid viscosity. The viscosity is defined as a function of the magnetic-field-dependent fluid yield stress, $\tau_y(H)$, and the local shear rate, $\dot{\gamma}$, computed in the CFD model. Several functions are used in the literature to define the viscosity such as Papanastasiou's model (Papanastasiou, 1987), Eyring model (Choi et al., 2005), hyperbolic tangent function (Case et al., 2013), or bi-viscous Bingham model (Ellam et al., 2006). However, the best results were obtained by using a blending equation that was developed by Susan-Resiga (2009). That is:

$$\eta = \eta_o \left[1 - \tanh\left(\frac{\dot{\gamma}}{\dot{\gamma}^*}\right)\right] + \left[\tau_y(H) + \tau_1 \left(\frac{\dot{\gamma}}{\dot{\gamma}^*}\right)^{1-n}\right] \tanh\left(\frac{\dot{\gamma}}{\dot{\gamma}^*}\right)/\dot{\gamma} \tag{3}$$

where, η_o, $\dot{\gamma}^*$, τ_1, and n are rheological parameters that control the growth of viscosity at very low shear rates, whose values are shown in Table 1 at the different input currents investigated in the current study. That function was found to fit the experimental measurements of the viscosity of the MR fluid used in the damper over a wide range of applied shear rates. It should be noted that the rheological shear stress-shear rate diagram is highly nonlinear and it differs for each type of MR fluid device, and also for the same MR fluid device at different magnetic fields. So, fitting an equation that describes the characteristic shear stress-shear rate diagram of an MR fluid requires equation parameters to be determined at different magnetic fields and fit a wide range of shear rates, as achieved by Susan-Resiga (2009). The bi-viscous Bingham model has been also investigated in the current study, as will be shown in Section 4.6. The apparent viscosity according to the bi-viscous Bingham model is defined as:

$$\eta = \begin{cases} \mu_s & \dot{\gamma} \le \dot{\gamma}_k \\ \mu_p + \frac{\tau_y}{\dot{\gamma}} & \dot{\gamma} > \dot{\gamma}_k \end{cases} \tag{4}$$

where μ_s is the maximum viscosity at the critical shear rate $\dot{\gamma}_k$, and μ_p is the plastic viscosity whose value is reported to be 100 to 1000 times less than the maximum viscosity (Parlak et al., 2012; Bullough et al., 2008). The maximum viscosity, which occurs at zero shear rate, is often referred to as the solid viscosity to denote the shear between the fluid and the solid plug formed. The values adopted for these parameters are also shown in Table 1.

The definition of fluid viscosity by a steady-state relation, $\eta = f(\tau_y(H), \dot{\gamma})$ as in Eqs. (3) and (4), includes modelling the viscoplastic behaviour of the fluid. To express the viscoelastic behaviour exerted by the fluid in the pre-yield zone, the yield stress should be expressed as a function of time. To do this, the following equation was used (Bullough et al., 2008):

$$\tau_y(t, H) = \tau_y(H)\left[1 - e^{-(G\dot{\gamma}t/\tau_y(H))}\right] \tag{5}$$

where, t is time and G is the fluid shear modulus, which can be defined as the ratio of shear stress to the shear strain (Lifshitz et al., 1986).

The magnetic field strength, H, is determined by the FE model, then the corresponding yield stress, $\tau_y(H)$, is defined in the CFD model according to the information obtained from the fluid data sheet (Lord Corporation, 2017). The fluid yield stress is fed as a text file that is read and processed by the UDF based on cell coordinates. Therefore, the UDF uses the fluid yield stress in conjunction with the local shear rate determined by the CFD solver to define the viscosity according to Eqs. (3) and (5).

3.3. Governing equations

The main governing equations of the magnetic field analysis are the well-known Maxwell's equations developed in the weak form (Purcell and Morin, 2013), given by the following equations:

$$\nabla.\vec{D} = \lambda \tag{6}$$

$$\nabla.\vec{B} = 0 \tag{7}$$

$$\nabla \times \vec{E} = -\frac{\partial \vec{B}}{\partial t} \tag{8}$$

$$\nabla \times \vec{H} = \vec{J} + \frac{\partial \vec{D}}{\partial t} \tag{9}$$

where $\vec{D}$ is the electric flux density, λ is the electric charge density, $\vec{B}$ is the magnetic flux density, $\vec{E}$ is the electric field intensity, $\vec{H}$ is the

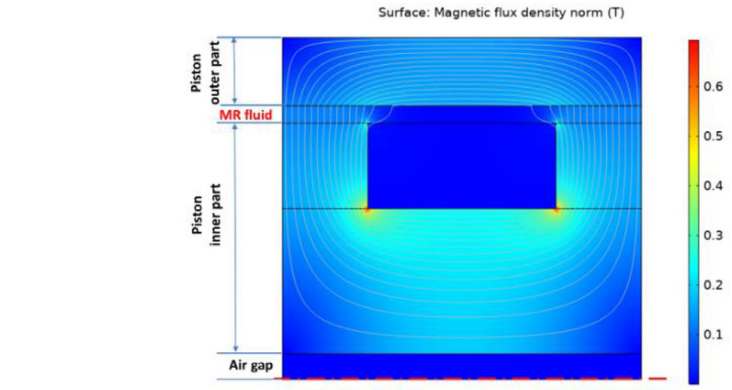

(a)

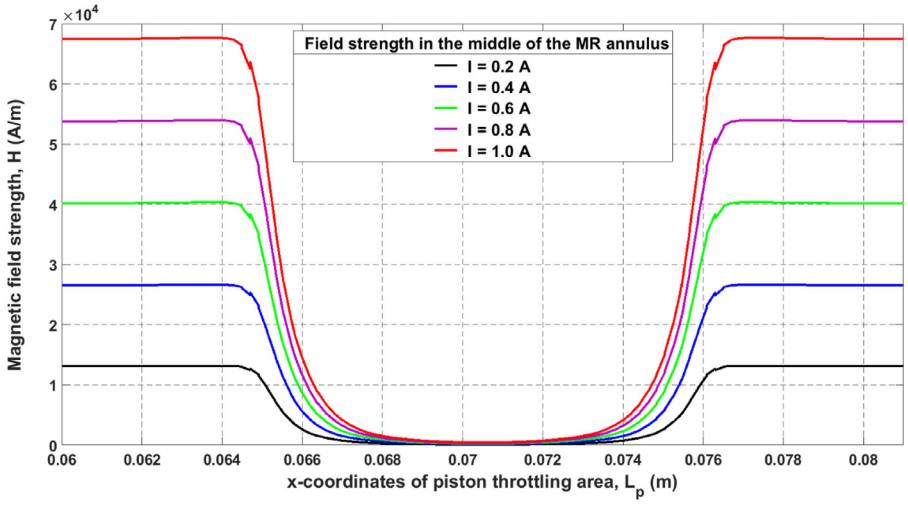

(b)

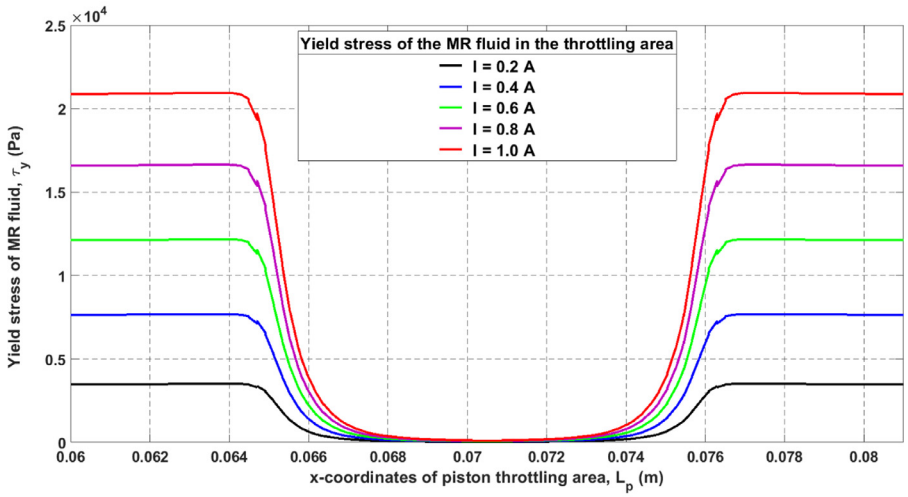

(c)

Fig. 5. Distribution of magnetic field in the MR piston and corresponding yield stress of the fluid: (a) contours of magnetic field density at $I = 0.2$ (A), (b) distribution of magnetic field intensity in the middle of the MR region at different input currents, and (c) corresponding yield stress of the fluid determined from the fluid data sheet (Lord Corporation, 2017).

magnetic field intensity (strength), and $\vec{J}$ is the current density. On the other hand, the main governing equations used in the fluid flow analysis are the continuity and momentum equations that are described in the VOF model, respectively, as follows:

$$\frac{1}{\rho_i}\left[\frac{\partial}{\partial t}\left(\alpha_i \rho_i\right) + \nabla.\left(\alpha_i \rho_i \vec{u}_i\right) = \dot{m}_{ij} - \dot{m}_{ji}\right] \tag{10}$$

$$\frac{\partial}{\partial t}\left(\rho_m \vec{u}_m\right) + \nabla.\left(\rho_m \vec{u}_m \vec{u}_m\right) = -\nabla p + \nabla .\vec{\tau} + \rho_m \vec{g} \tag{11}$$

where i and j represent the corresponding phase, α_i is the volume fraction of the corresponding phase, ρ_i is the density of each phase, $\vec{u}_i$ is the flow velocity vector of the corresponding phase, $\dot{m}_{ij}$ is the mass

Table 2
Parameters of the numerical approach.

Radius of the air gap, r_o	= 1.5 mm
Radius of the inner surface of the throttling area, r_1	= 15 mm
Radius of the outer surface of the throttling area, r_2	= 16 mm
Radius of piston core, r_3	= 10 mm
Outer radius of the, r_4	= 20 mm
Total length of the piston, L_{pis}	= 21 mm
Length of piston shoulders (magnetic poles), L_{pole}	= 5 mm
Type of fluid used	MRF-132 DG (Seid et al., 2018)
Material of the piston	SAE-1020 (Seid et al., 2018)
Electric conductivity of the MR fluid, σ_{MR}	= 10^{-11} S/m
Electric conductivity of SAE-1020, σ_p	= 8.41×10^6 S/m
Relative permeability of the MR fluid, μ_{rMR}	$B-H$ curve (Lord Corporation, 2017)
Relative permeability of Vacoflux-50, μ_{rp}	$B-H$ curve (Comsol, 2018)
Number of turns of each coil, n_T	= 150
MR fluid density at reference pressure, ρ_o	= 3050 kg/m^3
Reference bulk modulus, B_{ref}	= 6×10^6 Pa
density exponent, n	= 14
Height of the air pocket	= 10 mm
Total length of the damper	= 110 mm

transfer from phase i to phase j, $\vec{u}_m$ and ρ_m are the mass-averaged velocity and density of the mixture, respectively, p is the fluid pressure, $\vec{\tau} = f(\tau_y(H), \dot{\gamma})$ is the second-order deviatoric stress tensor, and $\vec{g}$ is the gravity acceleration.

It is worth mentioning that there are two approaches for numerical calculation of multiphase flows, namely: the Euler–Euler approach and the Euler–Lagrange approach (Ansys, 2009). In the Euler–Euler approach, to which the VOF model belongs, the different phases are treated as interpenetrating/immiscible continua. On the other hand, the Euler–Lagrange approach treats the fluid phase as a continuum, while the dispersed phase has the form of a large number of particles, bubbles or droplets, whose positions are tracked through the computational domain. There are three multiphase models available in the Euler–Euler approach, namely: VOF, Mixture model, and the Eulerian model. The VOF model is the model preferred when modelling a flow field that is represented by immiscible continua, in which the interface between the phases is initially known (Ansys, 2009; Adaze et al., 2019; Ho et al., 2011).

The density of the MR fluid is defined in ANSYS/Fluent by the simplified Tait equation assuming a linear growth of fluid bulk modulus, B, as a function of pressure. That is:

$$\left(\frac{\rho}{\rho_o}\right)^n = \frac{B_{ref} + n\,\Delta p}{B_{ref}} \tag{12}$$

where, B_{ref} is the reference bulk modulus taken as: $B_{ref} = 6\times10^6$ (Pa), and n is the density exponent taken as $n = 14$. The MR fluid density at the reference pressure is $\rho_o = 3050$ (kg/m^3).

Therefore, the governing equations of the CFD model are solved within the computational fluid domain shown in Fig. 3(b) so that the different flow parameters are determined. The fluid pressure in each chamber was used to determine the hydraulic force of the damper according to Eq. (1). The wet friction force was determined by the calculation of the total shear stress on piston walls multiplied by the side area of the piston, as in Syrakos et al. (2018) and Elsaady et al. (2020).

To summarise the current computational method, the FE and CFD models were established in the same manner presented in Elsaady et al. (2020). The FE model studies the flow of magnetic flux in the MR piston, shown in Fig. 1(b), based on Maxwell's equations using COMSOL/Multiphysics. The CFD model studies the MR fluid flow in the fluid domain of the damper using a two-phase flow model developed by the VOF model that is available in ANSYS/Fluent. The UDF couples both solvers by the definition of fluid viscosity in the CFD model according to Eq. (3) or (4), and Eq. (5). The value of the fluid yield stress, τ_y, in the equation is determined according to the magnetic field intensity determined by the FE model. The main parameters of the numerical approach are shown in Table 2, which also presents the main dimensions of the damper shown in Fig. 3(a) and (b).

4. Results and discussions

4.1. Results of the FE model

The steady-state contours of magnetic field density in the piston head of the MR damper at $I = 0.2$ A are shown in Fig. 5(a). It is seen that the main flow of the magnetic field in the MR fluid region occurs at the farthermost ends of the piston. The distributions of magnetic field intensity in the MR fluid region at different input currents is shown in Fig. 5(b), whereas the variation of the corresponding yield stress of the fluid is shown in Fig. 5(c). The fluid yield stress was determined by applying curve fitting of the $\tau_y - H$ diagram available in Lord Corporation, 2017).

4.2. Model validation

The current numerical approach has been validated by the direct comparison with experimental data presented in Section 2. The theoretical and experimental dynamic characteristics of the damper performance at different conditions are compared as shown in Figs. 6–8. The figures depict the dynamic characteristics of the damper at $I = 0.2$, 0.4, and 1 A, respectively, and the values of $f = 1$ Hz and $x_{amp} = 3$ mm for the sinusoidal motion of the piston. It is seen that the theoretical results nearly coincide with the experimental data, except for the sudden decrease of the force in the experimental data. These sudden cusps are reported in different studies such as Parlak and Engin (2012), Desai et al. (2019), Hudha et al. (2005), Yu et al. (2020), Ji et al. (2020) and Metered et al. (2010) and recently in Sapiński et al. (2020) for the same MR damper under investigation in the current study. However, the reason for their occurrence is proposed in this paper for the first time. The occurrence of these sudden cusps is thought to be mainly due to the dynamic effect of yield stress. In Figs. 6–8, at $t = 0$ and 0.5 s, the piston has instantaneous stops and starts to move either in the compression or rebound strokes, respectively. Therefore, the fluid is totally plugged in the MR fluid region at those moments, as also reported in Elsaady et al. (2020). When the piston starts to move, the plugged fluid in the MR fluid region moves with the piston as one body until a sufficient pressure difference of the fluid in both chambers is built up. Once this pressure difference occurs, the plug starts to break and this allows the fluid to flow in the region. However, this sudden flow causes an instantaneous drop in the pressure difference, which is indicated by the cusps seen on the force diagrams. It is thought that this instantaneous drop in the pressure difference between the chambers enables the reformation

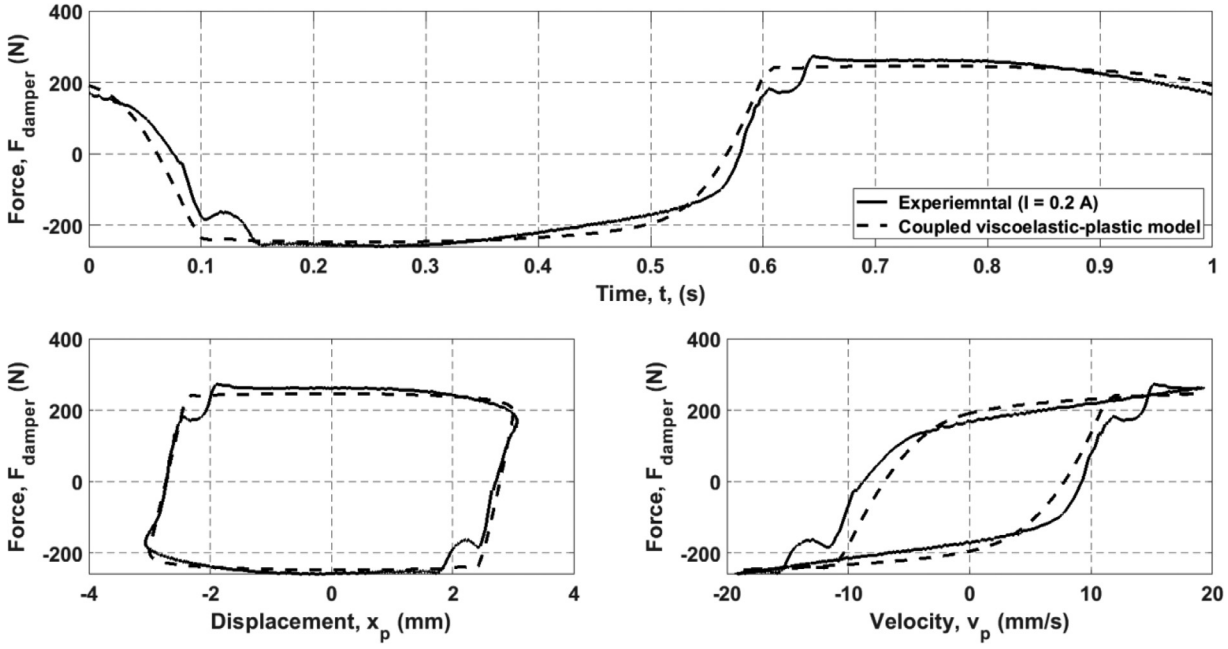

Fig. 6. Theoretical and experimental results of the dynamic characteristics of the RD-8040-1 MR damper: (up) force–time histories in a complete cycle at $I = 0.2$ A, $f = 1$ Hz, $x_{amp} = 3$ mm, (down-left) force–displacement diagrams, and (down-right) force–velocity diagrams.

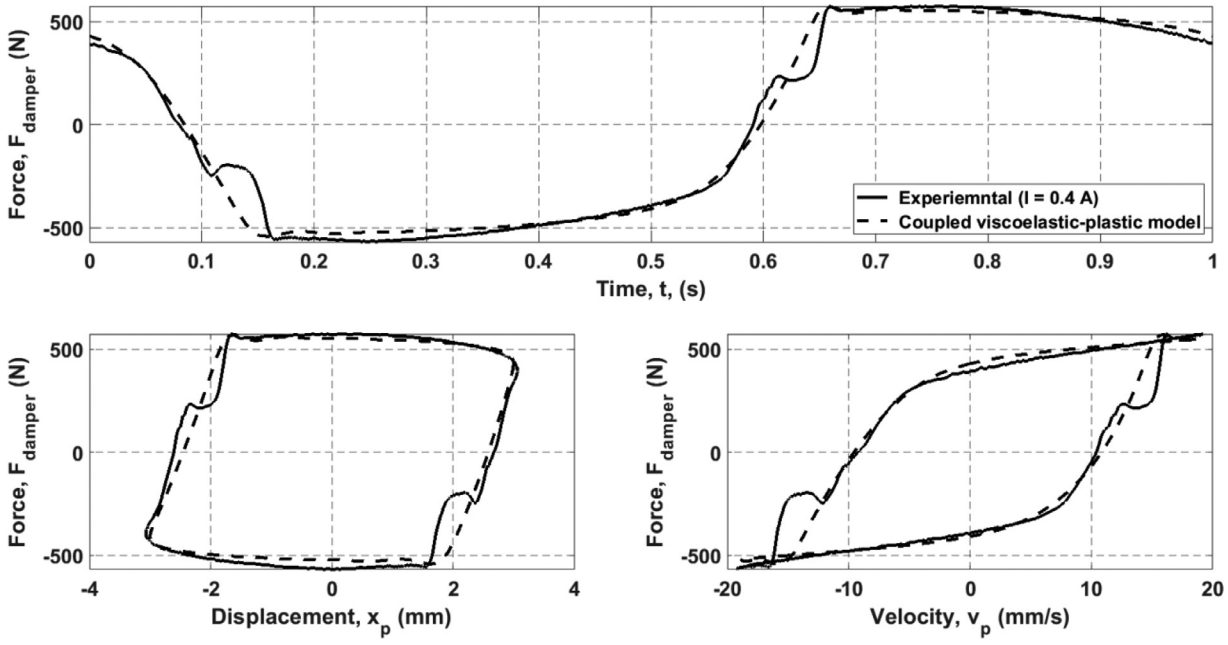

Fig. 7. Theoretical and experimental results of the dynamic characteristics of the RD-8040-1 MR damper at $I = 0.4$ A.

of fluid plug in the MR fluid zone. Hence, the pressure difference between the chambers is built up again until the plug is broken up again at the beginning of the plastic zones ($t \cong 0.15$ and 0.65 s). The occurrence of these sudden peaks is thought to be more reported with relatively low values of piston velocities. These peaks were not predicted by the current numerical approach as it is thought that more refining of the mesh and the time step is required such that this phenomenon can be modelled accurately.

4.3. Effect of fluid compressibility

Fluid compressibility is reported to cause the hysteretic behaviour of MR dampers, which can be described by the non-zero values of damper force at instantaneous locations of zero velocity, as shown in the force–velocity diagrams in Fig. 2 and Figs 6–8. The compressibility effects are due to the presence of air/gas chambers in most of the common designs of MR dampers. The relative volume of these air chambers lowers the effective bulk modulus of the fluid considerably. To investigate the effect of fluid compressibility in the current MR damper, the dynamic characteristics of the damper were determined based on the coupled numerical approach employing different values of fluid bulk modulus, as shown in Fig. 9. It is seen that the lower value of fluid bulk modulus leads to a wider hysteretic zone that is mostly noted in the characteristic force–velocity diagram. Therefore, it can be concluded that the compressibility effects are the main source of hysteretic behaviour of MR dampers, as also found by Guo et al. (2019).

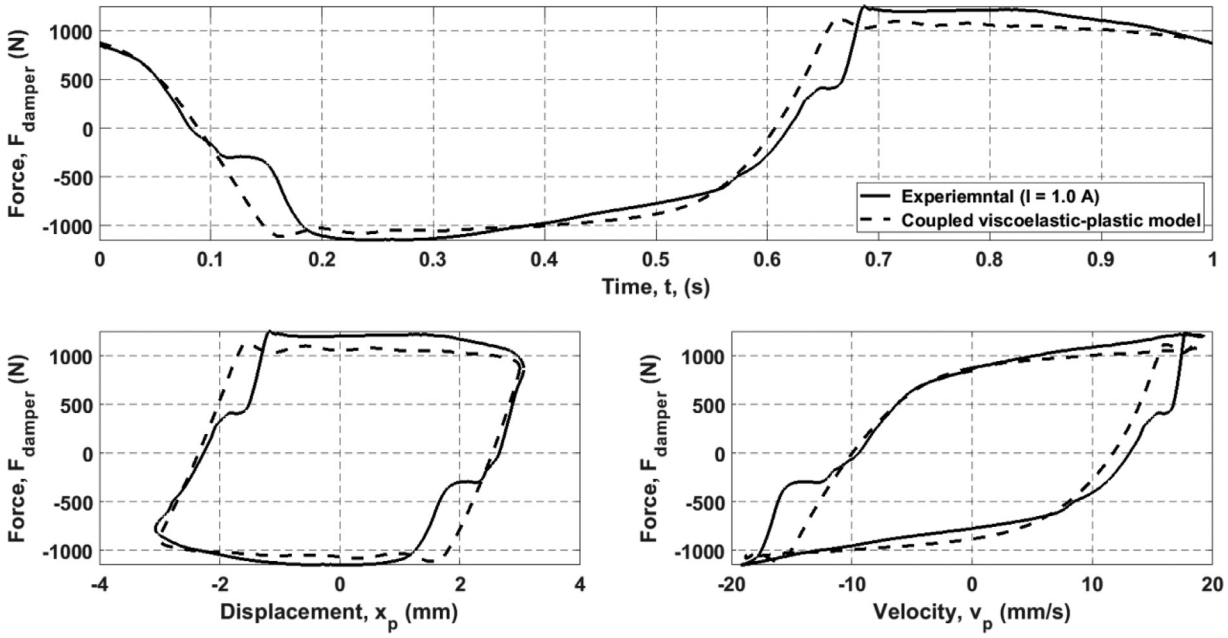

Fig. 8. Theoretical and experimental results of the dynamic characteristics of the RD-8040-1 MR damper at $I = 1.0$ A.

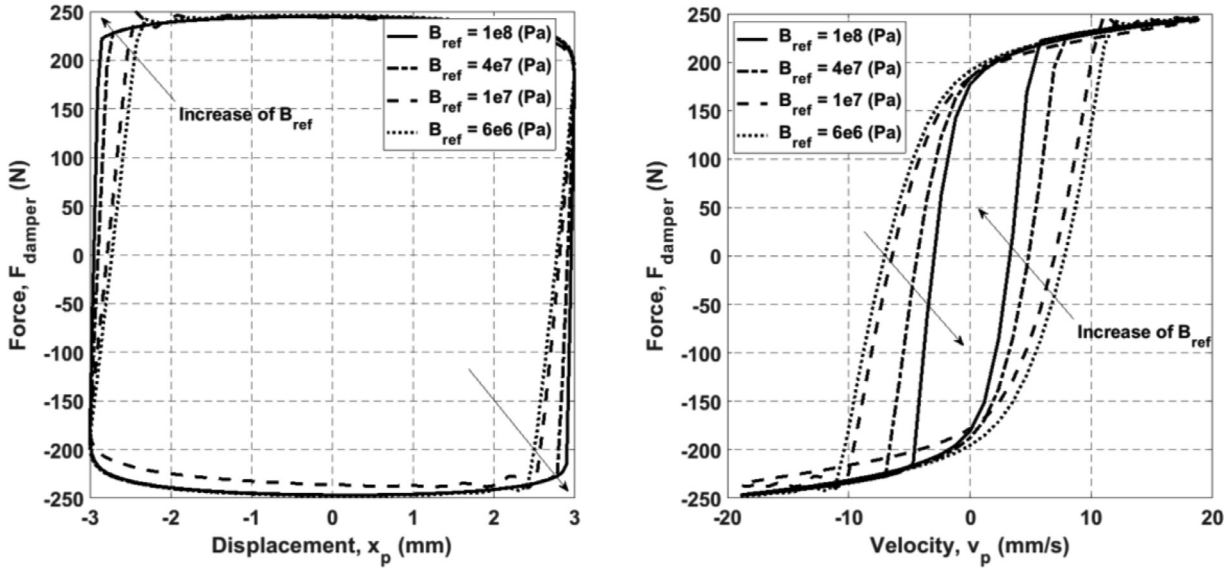

Fig. 9. Theoretical force–displacement diagrams (left), and force–velocity diagrams (right) for different values of the fluid bulk modulus.

4.4. *Effect of viscoelasticity*

The viscoelastic characteristics are mostly neglected in the study of MR dampers due to their minor effects and the difficulty presented in numerical simulations by their constitutive equations (Syrakos et al., 2018). However, it should be noted that the viscoelastic effects are remarkable and should not be neglected within MR dampers employing fluids with super high viscosity or high velocity of the piston (Syrakos et al., 2018). The viscoelastic characteristics are also reported to cause further hysteretic behaviour of MR dampers. The viscoelastic characteristics of MR fluids depend on the value of the shear modulus, G, shown in Eq. (5). The higher value of G indicates higher elastic properties, therefore the fluid nearly deforms plastically. The viscoelastic characteristics of MR fluids are measured by the determination of the value of G at different input currents, as in Chooi and Oyadiji (2005) and Li et al. (1999). The shear modulus is measured by applying an oscillatory strain to a sample of the MR fluid and measuring the resulting stress (Meyers and Chawla, 2008). The values of the shear modulus of MR fluids are reported to be in the range of $G = 10^5$ to 10^7 Pa (Chooi and Oyadiji, 2005).

To evaluate the viscoelastic characteristics in the current MR damper, the variation of pressure in the rebound chamber was predicted by the current numerical approach using different values of G, as shown in Fig. 10. The pressure is plotted only on a time interval of $T/4$, where $T = 1$ s, and it represents the period of oscillation. This time interval represents the piston motion in the compression stroke starting from rest at $t = 0$, until maximum velocity at $t = T/4$. The pressure in the rebound chamber mainly constitutes the damper output force. That is because the variation of pressure in the compression chamber is negligible due to the presence of the accumulator, as shown in Fig. 1(b). It is seen in Fig. 10 that the variation of pressure in the rebound chamber is achieved faster at higher values of G. The retardation of pressure

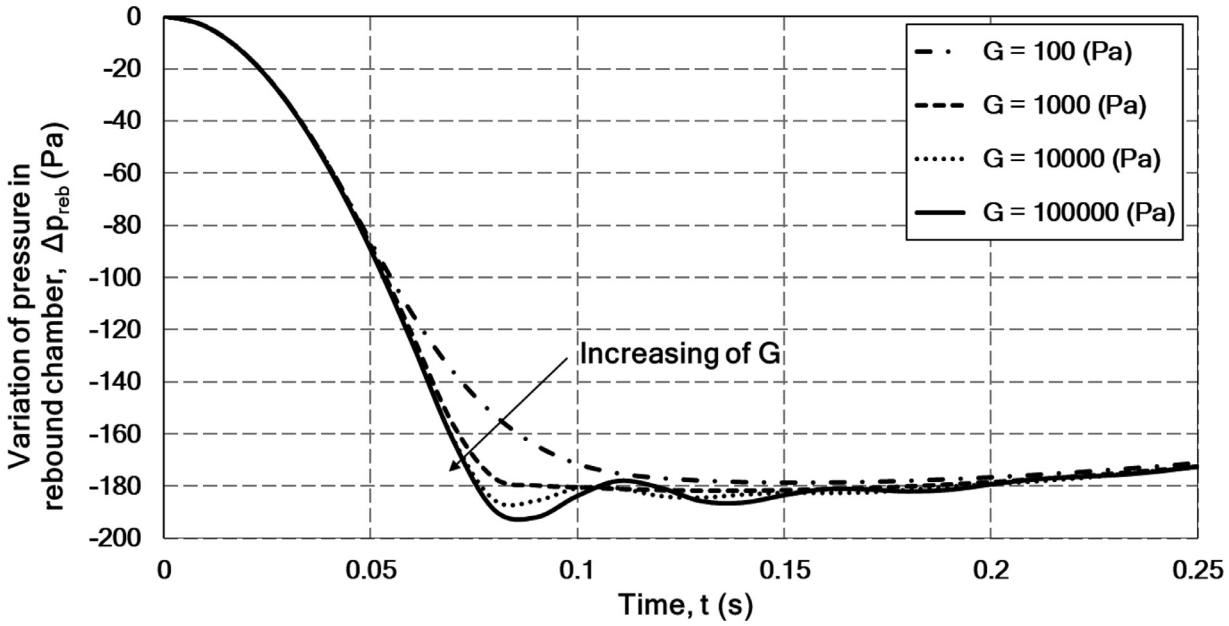

Fig. 10. Variation of pressure in the rebound chamber due to employing different values of G in the numerical approach, $B_{ref} = 1 \times 10^7$ Pa, $f = 1$ Hz.

decrease, which indicates wider hysteretic behaviour of the damper, is only seen at values of G lower than 100 Pa, which is considerably lower than the values reported for most MR fluids ($G = 10^5$ to 10^7 Pa). It was found that assuming G with higher values than 10^5 Pa leads to the same results as $G = 10^5$ Pa. Therefore, it can be concluded that the flow of MR fluids in MR dampers can be considered as a pure viscoplastic flow, as it is seen that the inclusion of viscoelastic characteristics nearly leads to the same results for high values of G. So, from the results presented in Figs. 9 and 10, it can be deduced that the prediction of the hysteretic behaviour of the current MR damper is mainly caused by the inclusion of compressibility effects of the fluid. In other words, the hysteretic behaviour of the current MR damper is due to fluid compressibility which is nonlinear elasticity, but not viscoelasticity. The definition of liquids as incompressible media is a quite common and acceptable assumption. However, in closed systems, the compressibility effects should be accounted for as the effective bulk modulus of the liquid-gas mixture is considerably low compared to the value of the bulk modulus of the fluid itself (Jelali, 2003). Also, it should be noted that the viscoelastic characteristics may be remarkable at higher frequencies and higher piston velocities and amplitudes.

To show the viscoelastic effect in the current MR damper, the variation of pressure in the rebound chamber was investigated at a high frequency of $f = 40$ Hz, as shown in Fig. 11. The pressures are also plotted in the time interval of $T/4$ for two values of G, and the reference bulk modulus was selected as a high value of 1×10^8 Pa, to minimise the effect of fluid compressibility. $B_{ref} = 1 \times 10^8$ Pa is the approximate value reported for silicone oil, which is the most common carrier fluid employed in MR fluids (Dow Corning, 2018). It is seen in Fig. 11 that employing different values of G leads to a considerable difference in the profile of pressure in the rebound chamber. The maximum difference between both curves was found to be 15% relative to the pressure at $G = 100$ Pa.

4.5. Effect of fluid inertia

The hysteretic behaviour of MR dampers is also attributed to the effects of fluid inertia. High piston velocity and high MR fluid density lead to a higher effect of fluid inertia. To evaluate the role of fluid inertia in the current damper, three cases with different values of motion frequency ($f = 1$, 10, and 20 Hz) were compared, as shown in Fig. 12. The values of motion amplitude and the applied current were kept constant in all cases. It is seen that the higher inertia effect of fluid caused by the piston motion with higher frequency leads to a wider hysteretic zone. Also, the higher frequency leads to an increase in the maximum force of the damper and causes variations of the curve at the beginning of the plastic zone (around $t = 0.1$ and 0.6 s) in the same manner presented in Guo et al. (2019). However, the inertial effects due to the variation of motion frequency are investigated in the current study, unlike the investigated inertial effects due to the variation of fluid density presented in Guo et al. (2019).

4.6. Effect of different rheological models employed in the numerical approach

There is a plethora of models that are used in numerical simulations to define the apparent viscosity of MR fluids, as shown earlier. So, it may be necessary to compare the theoretical predictions of the current approach according to different models of rheology. The theoretical output force of the damper due to the current model described by Eqs. (3) and (5) is compared with that force due to the bi-viscous Bingham model, defined by Eqs. (4) and (5), as shown in Fig. 13. It is seen that the current model describes the damper behaviour fairly accurately relative to the experimental data compared to the bi-viscous Bingham model. That is because the model developed by Susan-Resiga (2009) defined by Eqs. (3) and (5) is shown to describe the viscosity measurements for the MRF-132DG MR fluid, which is the fluid type employed in the damper, up to very high values of shear rate.

4.7. Visualisations of flow parameters

One of the benefits of the investigation of fluid flow by CFD techniques is the availability of visualisation of flow parameters. This helps in the better interpretation of flow characteristics, which is necessary especially in complicated flows, and developing new methods to improve system behaviours. To fully understand the characteristics of the rheological flow in the damper, the shear rate and viscosity contours in the throttling area of the damper are shown in Fig. 14(a) and (b), respectively, whereas the velocity vectors at two locations in the throttling area are shown in Fig. 15. The relation between the different parameters in both figures, namely: fluid shear rate, viscosity and velocity can be analysed. Fig. 14(a) shows the non-uniform distribution

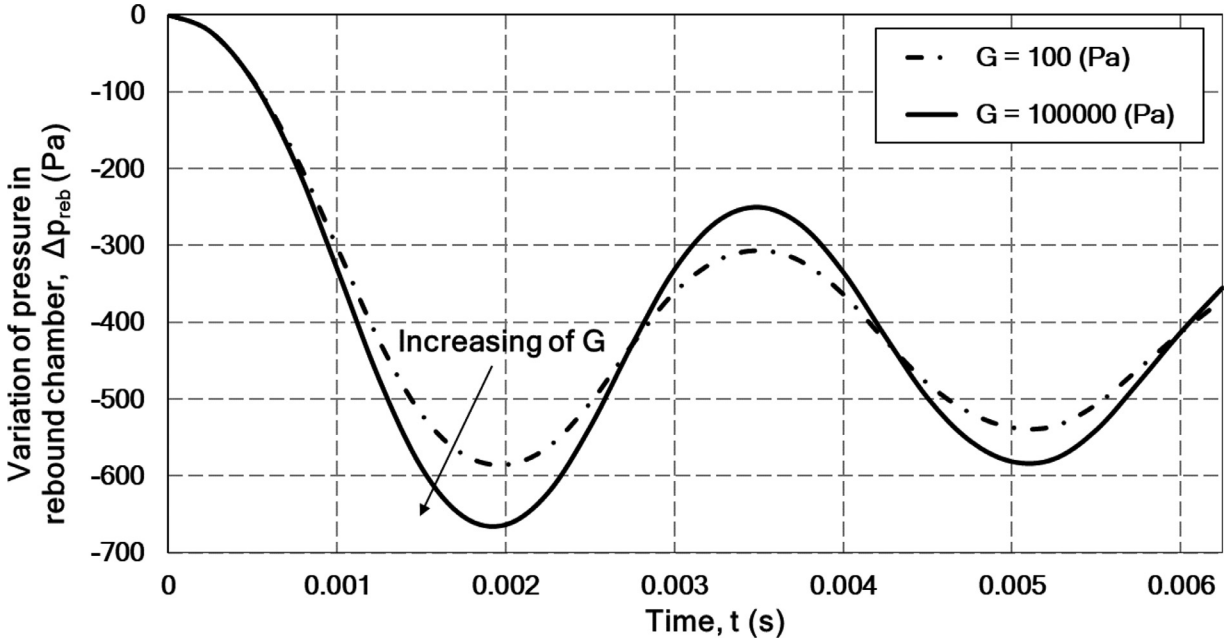

Fig. 11. Variation of pressure in the rebound chamber due to employing different values of G in the numerical approach, $B_{ref} = 1 \times 10^8$ Pa, $f = 40$ Hz.

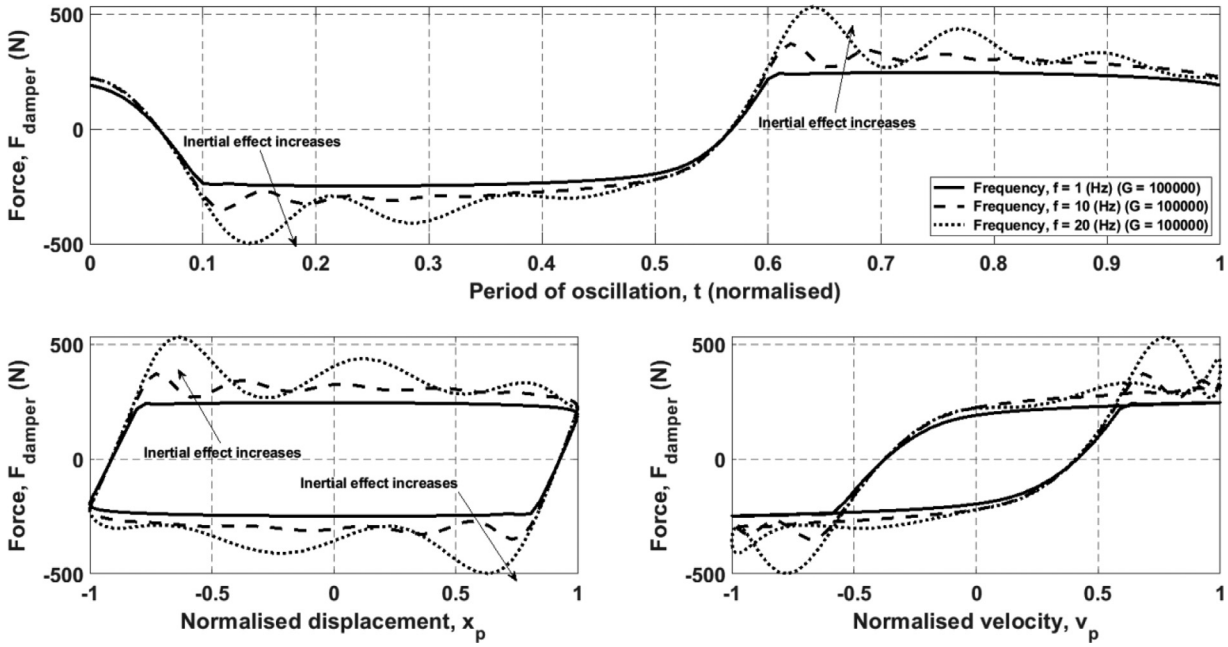

Fig. 12. Theoretical dynamic characteristics of the RD-8040-1 MR damper due to different motion frequencies, $I = 0.2$ A.

of the fluid viscosity due to the non-uniform distribution of the magnetic field. Also, the fluid viscosity is seen to be low at the outer and inner cylindrical surfaces of the throttling area. This is due to the high shear rate at these cylindrical surfaces, as seen in the zoomed areas in Fig. 14(b). It is also seen in Fig. 14(b) that the shear rate in the throttling area is approximately zero, since a plug flow profile is manifested, except for the outer and inner cylindrical surfaces of the throttling area. The shear rate is seen in those areas to be very high, which heightens the need for the accurate definition of the rheological model.

The variations of fluid viscosity and shear rate shown in Fig. 14 lead to a slight variation of the velocity profile along the MR fluid region, as shown in Fig. 15(a). The figure shows the velocity vectors at two locations in the throttling area: one of them is in the middle of the region adjacent to the left magnetic pole, Zone (A), whereas the other is in the middle of the throttling area (adjacent to the coil), Zone (B). It is seen that both velocity profiles are slightly different, as can be seen also in Fig. 15(b) which shows schematic drawings of the velocity profiles at the two locations. The velocity magnitude is slightly higher in the centre of Zone (B) compared to Zone (A). Also, the velocity magnitude is slightly lower in the outer and inner parts of Zone (B) compared to Zone (A). This difference is seen clearly in Fig. 15(a) in the zoomed areas that show the velocity vectors near the outer surface of the throttling area in the two zones. This indicates that the pre-yield region in the middle of the throttling area of the damper, Zone (B), is slightly smaller than that in the regions of magnetic poles, Zone (A), which is due to the relatively lower viscosity in Zone (B), as shown schematically in

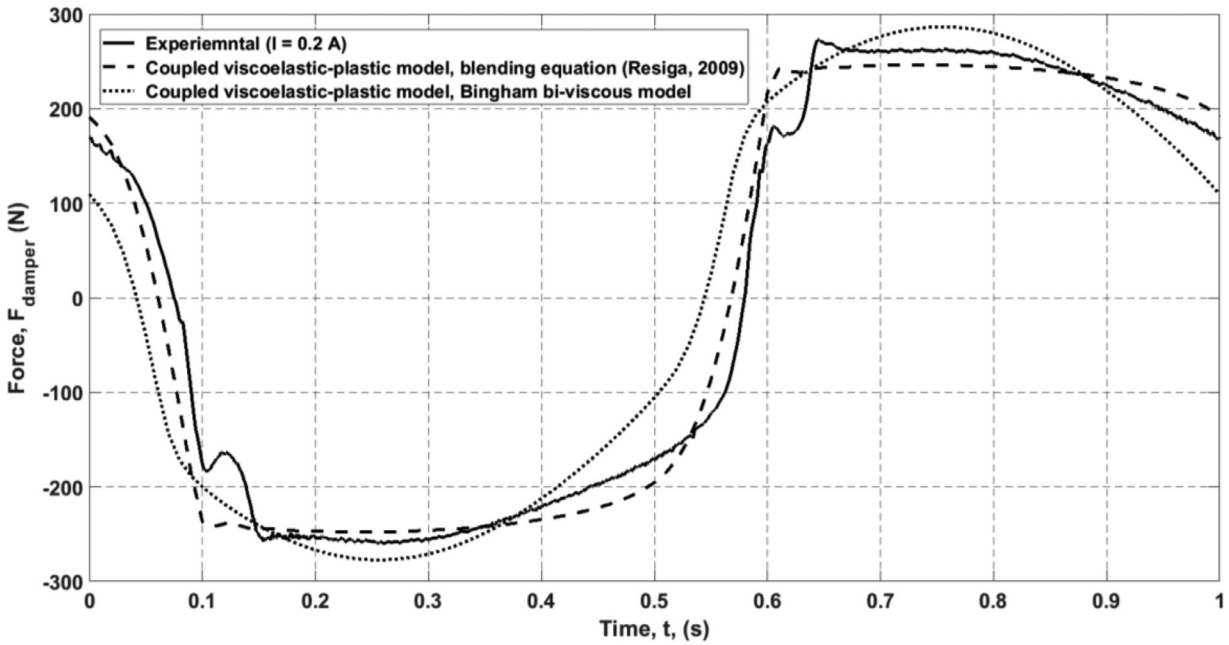

Fig. 13. Theoretical output forces of the damper due to the current model described by Eqs. (3) and (5), and the bi-viscous Bingham model in comparison with the experimental data.

Fig. 15(b). On the other hand, the post-yield region is slightly larger in Zone (B) compared to Zone (A). It is seen that both of the velocity profiles in the two regions are slightly different, although the magnetic field intensity is considerably high in Zone (A) compared to Zone (B). The reason for that slight difference is due to the fact that the fluid shear rate in the whole MR fluid region is approximately zero as shown earlier. Therefore, the MR effect is manifested in the MR fluid region adjacent to the coil, even if the applied magnetic field is small. Also, the zoomed areas in Fig. 15(a) also indicate that the velocity profile in the throttling area has common characteristics between Poiseuille and Couette flows, as also illustrated in Syrakos et al. (2018), Bullough et al. (2008) and Bhatnagar (2013). The main flow is a Poiseuille flow due to the pressure difference along the throttling area, whereas the Couette flow is seen at the edges of the throttling area at which a tiny portion of the fluid moves with the walls in the opposite direction of the main flow due to the non-slip boundary condition.

Referring to Figs. 14 and 15, it is worth mentioning that the prediction of the variation of fluid viscosity and shear rate, Fig. 14(a) and (b), respectively, and the variation of velocity profile, Fig. 15, along the MR fluid region is due to the non-uniform distribution of magnetic field intensity in the MR fluid region shown in Fig.5(b). The effect of that non-uniform distribution has been accounted for in the current CFD model, using the same technique presented in Kemerli et al. (2018) and Elsaady et al. (2020). Therefore, the fluid yield stress along the MR fluid region has also a non-uniform distribution, as shown in Fig. 5(c). In some previous studies such as Guo et al. (2019) and Parlak et al. (2012), the magnetic field intensity/density was only defined at the locations of magnetic poles, therefore, the variation of the magnetic field in the middle region was not accounted for. Alternatively, a homogenous magnetic field intensity/density in the whole MR fluid region was considered in Gurubasavaraju et al. (2018) and Guo and Xie (2019), therefore, the whole MR fluid region is affected by a uniform yield stress, whose value is determined according to the average magnetic field intensity/density. However, the current numerical approach accounts for the non-uniform distribution of fluid yield stress, as performed in Kemerli et al. (2018, 2019). That is because the profile of yield stress shown in Fig. 5(c) has been defined as a 2D array based on the coordinates of the MR fluid region using a text file that is compiled by the UDF.

5. Investigation of the off-state dry friction force

In the preceding modelling approach presented in Sections 3 and 4, it has been shown that the fluid compressibility and inertia are the main reasons for the hysteretic behaviour of the current MR damper, as shown in Figs. 9 and 12, respectively. The effect of viscoelasticity was found to be minor. The friction forces are also reported to contribute to the hysteretic behaviours of MR dampers. The effect of wet friction has been included in the current numerical approach by the determination of shear stresses on piston walls. On the other hand, the effect of dry friction of the piston rod with the sealing glands was neglected, as in many numerical and multi-physics analyses that are presented in Gurubasavaraju et al. (2018), Guo and Xie (2019), Syrakos et al. (2018), Meng et al. (2017) and Wang et al. (2017). However, because the dry friction is reported to produce the hysteretic behaviours of hydraulic dampers (Heipl and Murrenhoff, 2015; Gagnon et al., 2020; Zhao and Xu, 2018), therefore, it merits to be investigated in this study, as the study investigates the nonlinear phenomena that lead to the hysteretic behaviour of MR dampers.

It should be noted that the dry friction resistance in hydraulic dampers subjected to reciprocal loads is also a nonlinear dynamic behaviour, as shown by Heipl and Murrenhoff (Heipl and Murrenhoff, 2015). In that paper, the dynamic dry friction resistance to the reciprocal motion of the piston rod in the hydraulic cylinder was measured for different kinds of seals. They illustrated the difference between dynamic and steady-state friction resistance, as shown in Fig. 16. It is seen that the dynamic resistance manifests a hysteretic loop, whereas the steady-state behaviour does not. That hysteretic loop is also reported in MR dampers in both off- and on-states, as shown in Zhao and Xu (2018), in which the hysteresis of MR dampers was modelled taking into consideration the Stribeck curve. The Stribeck curve is a fundamental concept in tribology which defines the friction between sliding surfaces in relative motion (Heipl and Murrenhoff, 2015).

The hysteretic loops are also seen in the dynamic characterisation of the current MR damper even in the off-state, as shown in Fig. 2. The off-state hysteretic loops are also reported in Sapiński et al. (2020) for the same MR damper under investigation in the current study. Therefore, that off-state hysteretic behaviour can be attributed to viscous, inertia,

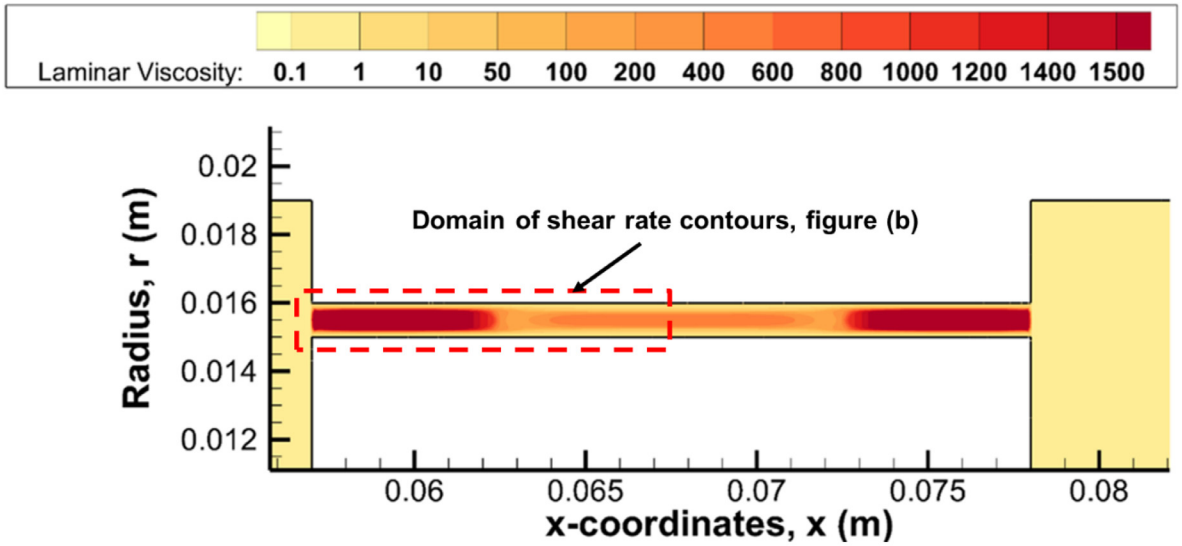

(a)

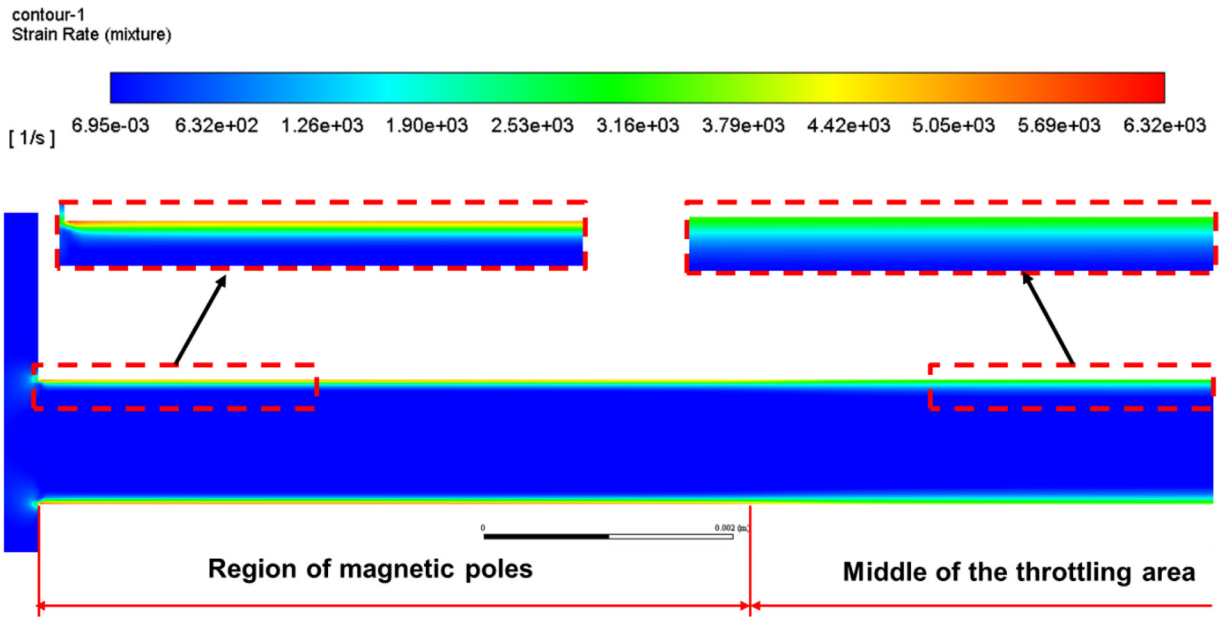

(b)

Fig. 14. Viscosity, (a), and shear rate, (b), contours in the throttling arear of the damper at $t = T/4 = 0.25$ s (maximum velocity of the piston in the right-to-left direction).

compressibility and friction effects. In order to evaluate the role of each element in producing the damper force and the corresponding hysteretic behaviour, the damper behaviour in the off-state has been modelled using the current CFD model. The CFD model was used to determine the damper behaviour due to the effects of pressure and viscous forces, gas compression, and fluid inertia. Therefore, the effects of dry friction and piston inertia can be evaluated by the difference between the experimental dynamic characteristics of the damper in the off-state shown in Fig. 2, and the theoretical results of the preceding forces.

Hence, the CFD model presented in Section 3 has been modified to study the performance of the damper in the off-state. The only modification was to the definition of fluid viscosity. Rather than the localised definition of fluid viscosity based on cell coordinates using the UDF to assign the magnetically activated and non-activated regions, as shown in Section 3.2, another homogenous definition of fluid viscosity was adopted. The fluid viscosity has been defined in the CFD model using the built-in library for Herschel–Bulkley fluids that is available in ANSYS/Fluent. The fluid was considered as a non-Newtonian fluid, even in the off-state, in the light of the off-state shear stress – shear rate diagram that is available in the fluid datasheet (Lord Corporation, 2017). The diagram shows a nonlinear profile, in which the fluid manifests a non-zero value of yield stress, whose magnitude is approximately 10 Pa, at zero shear rate. Therefore, the built-in Herschel–Bulkley model in ANSYS/Fluent was adopted, and the parameters of the model were assigned

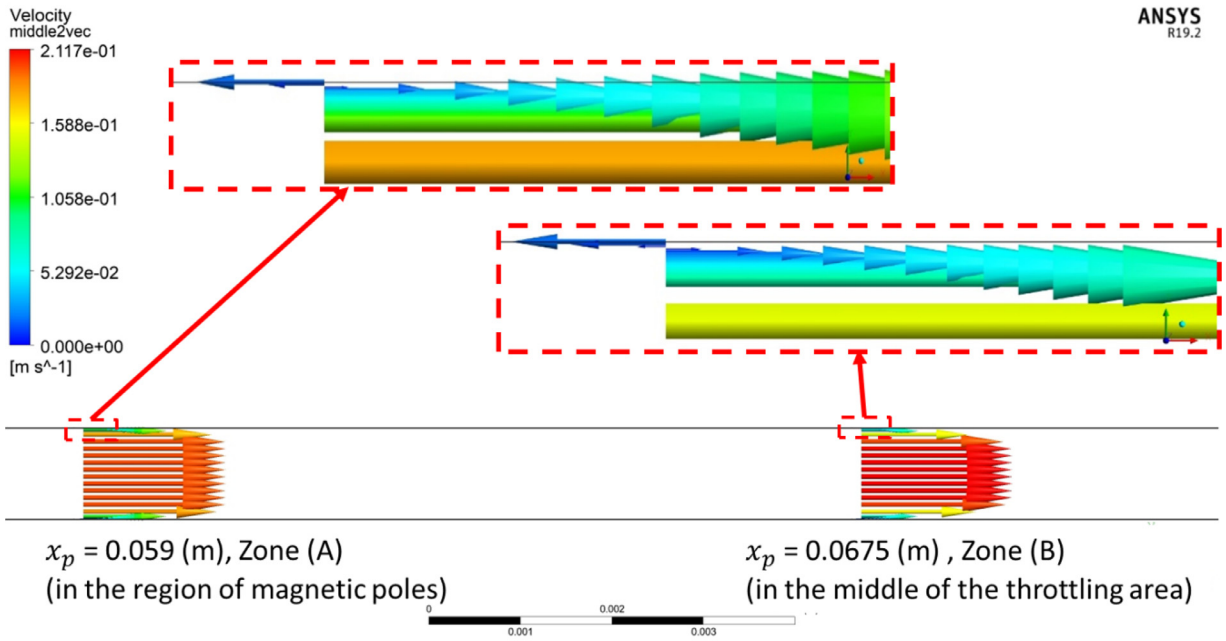

(a)

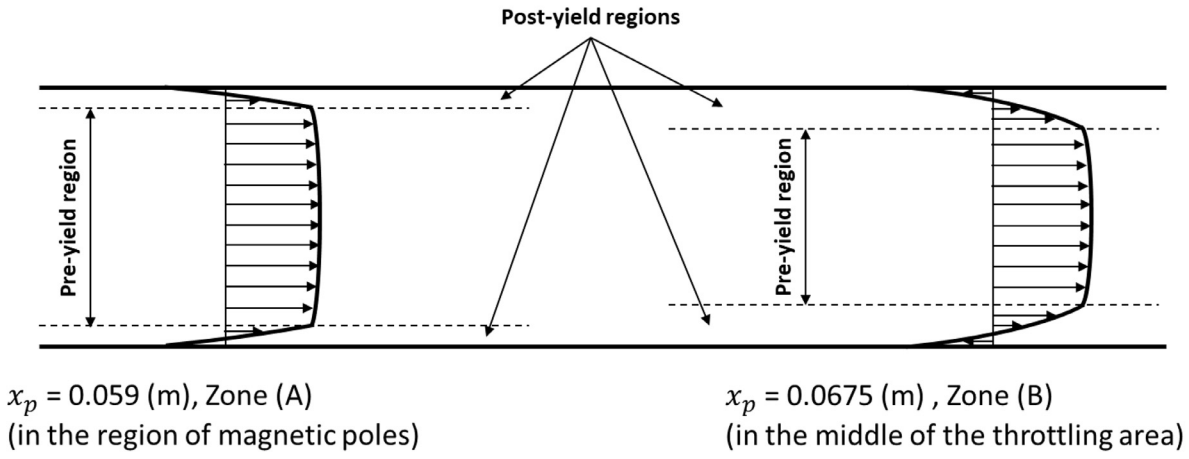

(b)

Fig. 15. Velocity vectors at two locations in the throttling area of the damper; one of them is in the middle of the region of the left magnetic pole, whereas the other is in the middle of the throttling area: (a) velocity vectors shown in the CFD solver, and (b) schematic drawings of the velocity profiles.

so that the viscosity equation according to the model fits the experimental flow curve of the fluid in the off-state that is available in the fluid datasheet (Lord Corporation, 2017). The built-in Herschel–Bulkley model in ANSYS/Fluent employs a bi-viscous definition of fluid viscosity that can be described by the following equations (Ansys, 2009):

$$\eta = \begin{cases} \tau_y\left(\frac{2-\dot{\gamma}/\dot{\gamma}_k}{\dot{\gamma}_k}\right) + k\left[\left(2-n_{HB}\right) + \left(n_{HB}-1\right)\frac{\dot{\gamma}}{\dot{\gamma}_k}\right] & \dot{\gamma} \le \dot{\gamma}_k \\ \frac{\tau_y}{\dot{\gamma}} + k\left(\frac{\dot{\gamma}}{\dot{\gamma}_k}\right)^{\left(n_{HB}-1\right)} & \dot{\gamma} > \dot{\gamma}_k \end{cases} \tag{13}$$

where k is the consistency index and n_{HB} is the flow index. The values of the constants shown in the preceding equation that were found to fit the experimental flow curve of the fluid (Lord Corporation, 2017) were as follows: $k = 0.41$ Pa.s, $n_{HB} = 0.88$, $\tau_y = 10$ Pa, and $\dot{\gamma}_k = 0.01$ Pa.s.

The CFD simulation has been performed and the same conditions of piston motion and the other solver settings were also applied. Hence, the theoretical output force of the damper due to pressure and viscous forces have been determined using Eqs. (1) and (2). The different elements of damper force, namely: the pressure and viscous forces according to the CFD model and the dynamic force due to gas compression are compared with the total force of the damper, as shown in Fig. 17. The difference between the experimentally-determined total force of the damper (black) and the total fluid forces predicted (blue) represents the role of the dry friction and the inertia force of the piston. It is seen that the total force of the damper is dominated by the dry friction and inertia force of the piston, rather than the pressure, viscous and dynamic gas forces. The maximum value of the pressure, viscous and dynamic gas forces

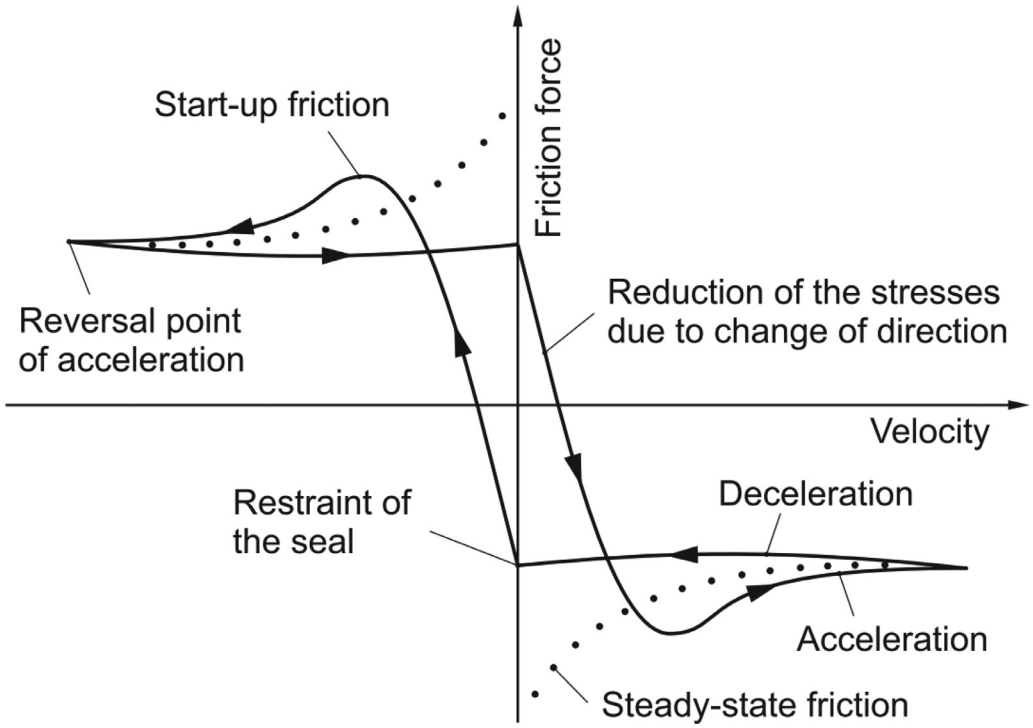

Fig. 16. Difference between dynamic and steady-state friction resistance for hydraulic dampers subjected to reciprocal loads (Heipl and Murrenhoff, 2015).

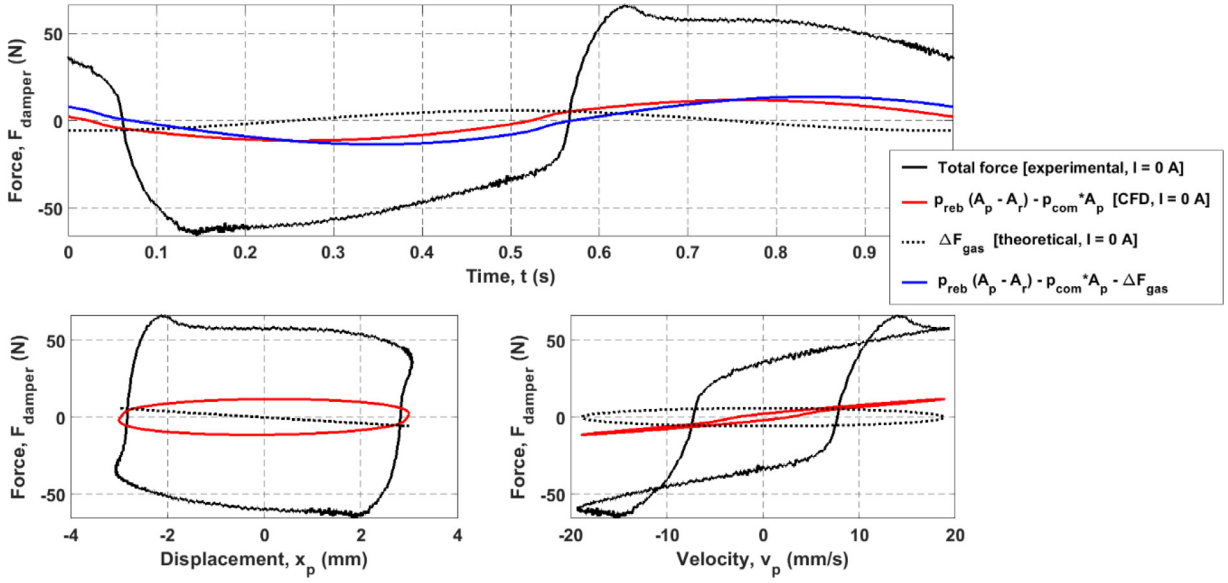

Fig. 17. Predictions of the theoretical pressure and viscous forces according to the CFD model, $p_{reb}(A_p - A_r) - p_{com}A_p$, and gas forces computed by Eq. (2), ΔF_{gas}, in comparison with the total experimental force of the damper. The difference between the total experimental force (black) and the total theoretical forces (blue) represents the total dry friction and inertia force of the damper.

represents about 21 % of the experimentally-determined total force of the damper.

A similar analysis to that described by Fig. 17 was presented in Zhao and Xu (2018), in which the forces due to pressure, viscous and dynamic gas forces were found to represent about 18% of the total damper force. Therefore, it can be concluded that the main output force of MR dampers operated in the off-state under low values of frequency and amplitude is dominated by the dry friction and inertial effects. The magnitude of the dry friction is influenced by the magnitude of the high pre-charge pressure that is required to avoid cavitation problems in the damper. The gauge value of pressure in the damper at the locations of sealing controls the static and dynamic friction resistance to the piston motion. Also, it can be deduced that the hysteretic behaviour due to these effects is remarkable in comparison with those manifested by the compressibility effects, as can be seen in the characteristic diagrams shown in Fig. 17. It is seen that a small hysteresis loop is manifested due to the pressure and viscous forces as determined by the CFD model, whereas the hysteresis loop manifested due to the experimental measurements is considerably wider.

In fact, compressibility effects are reported to cause nonlinear behaviour of different closed systems, including hysteretic behaviours of MR dampers (Goldasz, 2019; Guo et al., 2019; Jelali, 2003;

Stanway, 2004; Wang et al., 2010). The compressibility effects are related to the presence of air/gas chamber in MR dampers. However, it is thought that the yield stress of the MR fluid itself causes further effects of fluid compressibility. That is because there is a minimum pressure difference between the chambers of the damper required to initiate flow between the chambers. While the piston is moving and that threshold value of pressure difference is not achieved, the compressibility effects are manifested by the fluid-gas mixture. For instance in the compression stroke, the MR fluid compresses the air chamber and a gas pocket is formed in the rebound stroke, until a sufficient pressure difference between the fluid in both chambers is achieved, therefore the flow from the compression to rebound chamber starts in response to that pressure difference. As this pressure difference is directly proportional to the applied current, the time lag of the flow of the MR fluid in the throttling area increases. Therefore, wider hysteretic loops are manifested as the applied current increases, as seen in the characteristic diagrams shown in Fig. 2.

6. Conclusions

The performance of a commercially-available MR damper has been studied using theoretical and experimental methods. The theoretical method incorporates a coupled numerical approach between FE and CFD analyses. The CFD model allows better assessment of the characteristics of fluid flow which helps in design optimisation. It can be concluded that the frictional, compressibility and inertial and effects are found to mainly form the hysteretic behaviour of the MR damper, whereas the viscoelastic effects are minor. Also, the selection of the rheological model used to define the fluid viscosity is critical, as it leads to major differences in the predictions of the numerical approach.

The current numerical approach is thought to be useful not only to model the performance of MR dampers but also to model nonlinear performances of different MR fluid devices. That is because the current numerical approach presents a coupled analysis between magnetic and fluid flow analyses, in which different sources of nonlinearity are accounted for, namely: magnetic saturation, non-uniform distribution of magnetic field, and effects of fluid compressibility, viscoelasticity, inertia, friction, and presence of an air pocket. Modelling the performance of other MR fluid devices can be performed by changing the boundary conditions according to the problem description in each device, and follow the same strategy of the current numerical approach. Future work includes applying the same method on other MR fluid devices and investigations of two-way coupling methods.

Declaration of Competing Interest

The authors declare that they have no known competing financial interests or personal relationships that could have appeared to influence the work reported in this paper.

References

Adaze, E., Al-Sarkhi, A., Badr, H.M., et al., 2019. Current status of CFD modeling of liquid loading phenomena in gas wells: a literature review. J. Pet. Explor. Prod. Technol. 9 (2), 1397–1411. doi:10.1007/s13202-018-0534-4.

Ahamed, R., Choi, S.-B., Ferdaus, M.M., 2018. A state of art on magneto-rheological materials and their potential applications. J. Intell. Mater. Syst. Struct. 29 (10), 2051–2095. doi:10.1177/1045389X18754350.

Ahmadian, M., Norris, J.A., 2008. Experimental analysis of magnetorheological dampers when subjected to impact and shock loading. Commun. Nonlinear Sci. Numer. Simul. 13 (9), 1978–1985. doi:10.1016/j.cnsns.2007.03.028.

Ansys, 2009. ANSYS FLUENT 12.0 Theory Guide. ANSYS, Inc., United States.

Bhatnagar, R.M., 2013. Transient effect modelling of magnetorheological fluid–based damper at low speed and its comparison with the existing magnetorheological damper models. J. Intell. Mater. Syst. Struct. 24 (12), 1506–1523. doi:10.1177/1045389x12474355.

Bulea, T.C., Kobetic, R., To, C.S., et al., 2012. A variable impedance knee mechanism for controlled stance flexion during pathological gait. IEEE/ASME Trans. Mechatron. 17 (5), 822–832. doi:10.1109/TMECH.2011.2131148.

Bullough, W., Ellam, D., Wong, A., et al., 2008. Computational fluid dynamics in the flow of ERF/MRF in control devices and of oil through piezo-hydraulic valves. Comput. Struct. 86 (3-5), 266–280. doi:10.1016/j.compstruc.2007.01.043.

Cantelli, A., 2009. Uniform flow of modified Bingham fluids in narrow cross sections. J. Hydraul. Eng. 135 (8), 640–650.

Case, D., Taheri, B., Richer, E., 2013. Multiphysics modeling of magnetorheological dampers. Int. J. Multiphys. 7 (1), 61–76. doi:10.1260/1750-9548.7.1.61.

Case, D., Taheri, B., Richer, E., 2014. Dynamical modeling and experimental study of a small-scale magnetorheological damper. IEEE/ASME Trans. Mechatron. 19 (3), 1015–1024. doi:10.1109/TMECH.2013.2265701.

Chen, G., 2014. Chapter 3 – Fundamentals of contact mechanics and friction. In: Chen, G. (Ed.), Handbook of Friction-Vibration Interactions. Woodhead Publishing, Cambridge, UK, pp. 71–152.

Choi, Y.-T., Bitman, L., Wereley, N.M., 2005. Nondimensional analysis of electrorheological dampers using an eyring constitutive relationship. J. Intell. Mater. Syst. Struct. 16 (5), 383–394. doi:10.1177/1045389x05050529.

Chooi, W.W., 2005. Experimental Characterisation of the Properties of Magnetorheological (MR) Fluids and MR Damper PhD Thesis. The University of Manchester, UK.

Chooi, W.W., Oyadiji, S.O., 2005. Characterizing the effect of temperature and magnetic field strengths on the complex shear modulus properties of magnetorheological (MR) fluids. Int. J. Mod. Phys. B 19 (07n09), 1318–1324. doi:10.1142/S0217979205030244.

Chooi, W.W., Oyadiji, S.O., 2009. Experimental testing and validation of a magnetorheological (MR) damper model. J. Vib. Acoust. 131 (6), 061003. doi:10.1115/1.3142885.

Comsol, 2018. COMSOL Multiphysics Reference Manual. COMSOL Inc, Sweden.

Desai, R.M., Jamadar, M.E.H., Kumar, H., et al., 2019. Evaluation of a commercial MR damper for application in semi-active suspension. SN Appl. Sci. 1 (9), 993. doi:10.1007/s42452-019-1026-y.

Dominguez, A., Sedaghati, R., Stiharu, I., 2008. Modeling and application of MR dampers in semi-adaptive structures. Comput. Struct. 86 (3-5), 407–415. doi:10.1016/j.compstruc.2007.02.010.

Dow Corning, 2018. Compressibility Data. Data supplied by the company on 22 November 2018.

Ellam, D.J., Atkin, R.J., Bullough, W.A., 2006. Analysis of a smart clutch with cooling flow using two-dimensional Bingham plastic analysis and computational fluid dynamics. Proc. Inst. Mech. Eng. Part A J. Power Energy 219 (8), 639–652. doi:10.1243/095765005x31306.

Elsaady, W., Ibrahim, A., Abdalla, A., 2019. Numerical simulation of flow field in coaxial tank gun recoil damper. Adv. Mil. Technol. 14 (1), 139–150.

Elsaady, W., Oyadiji, S.O., Nasser, A., 2020. A one-way coupled numerical magnetic field and CFD simulation of viscoplastic compressible fluids in MR dampers. Int. J. Mech. Sci. 167, 105265. doi:10.1016/j.ijmecsci.2019.105265.

Elsaady, W., Oyadiji, S.O., Nasser, A., 2020. A review on multi-physics numerical modelling in different applications of magnetorheological fluids. J. Intell. Mater. Syst. Struct. 31 (16), 1855–1897. doi:10.1177/1045389x20935632.

Gagnon, L., Morandini, M., Ghiringhelli, G.L., 2020. A review of friction damping modeling and testing. Arch. Appl. Mech. 90 (1), 107–126. doi:10.1007/s00419-019-01600-6.

Goldasz, J., 2019. Chapter 4 – Developments in modeling of magnetorheological actuators. In: Choi, S.-B., Li, W. (Eds.), Magnetorheological Materials and their Applications. The Institution of Engineering and Technology, UK, pp. 63–91.

Gołdasz, J., Sapinski, B., Jastrzębski, Ł., 2018. Assessment of the magnetic hysteretic behaviour of MR dampers through sensorless measurements. Shock Vib. 2018, 21. doi:10.1155/2018/3740208.

Guo, P., Xie, J., 2019. Two-dimensional CFD modeling of hysteresis behavior of MR dampers. Shock Vib. 2019, 14. doi:10.1155/2019/9383047.

Guo, P., Xie, J., Dong, X., et al., 2019. A two-dimensional axisymmetric finite element analysis of coupled inertial-viscous-frictional-elastic transients in magnetorheological dampers using the compressible Herschel-Bulkley fluid model. Front. Mater. 6, 293. doi:10.3389/fmats.2019.00293.

Gurubasavaraju, M., Kumar, H., Mahalingam, A., 2018a. Performance analysis of a semi-active suspension system using coupled CFD-FEA based non-parametric modeling of low capacity shear mode monotube MR damper. Proc. Inst. Mech. Eng. Part D J. Automob. Eng. 233 (5), 1214–1231. doi:10.1177/0954407018765899.

Gurubasavaraju, M., Kumar, H., Mahalingam, A., 2018b. An approach for characterizing twin-tube shear-mode magnetorheological damper through coupled FE and CFD analysis. J. Braz. Soc. Mech. Sci. Eng. 40 (3), 1–14. doi:10.1007/s40430-018-1066-z.

Heipl, O., Murrenhoff, H., 2015. Friction of hydraulic rod seals at high velocities. Tribol. Int. 85, 66–73. doi:10.1016/j.triboint.2015.01.002.

Ho, C.-D., Chang, H., Chen, H.-J., et al., 2011. CFD simulation of the two-phase flow for a falling film microreactor. Int. J. Heat Mass Transf. 54 (15-16), 3740–3748. doi:10.1016/j.ijheatmasstransfer.2011.03.015.

Hudha, K., Jamaluddin, H., Samin, P., et al., 2005. Effects of control techniques and damper constraint on the performance of a semi-active magnetorheological damper. Int. J. Veh. Auton. Syst. 3, 230–252. doi:10.1504/IJVAS.2005.008235.

Jelali, M., 2003. Chapter 3 – Physical properties of fluids. In: Kroll, A. (Ed.), Hydraulic Servo-Systems: Modelling, Identification, and Control. Springer, London, UK, pp. 30–51.

H. Ji, Y. Huang, S. Nie, et al., Research on Semi-Active Vibration Control of Pipeline Based on Magneto-Rheological Damper, 10 (7) (2020), p. 2541.

Kemerli, M., Engin, T., Parlak, Z., 2018. A new rheological model of magnetorheological fluids for CFD: comparison and validation.. In: Proceedings of the ASME 2018 Conference on Smart Materials, Adaptive Structures and Intelligent Systems, San Antonio, USA. ASME, USA, p. 7984. doi:10.1115/smasis2018-7984 10-12 September.

Kemerli, M., Engin, T., Parlak, Z., 2019. Coupled magnetic and CFD modelling of a structural magnetorheological vibration absorber with experimental validation. Mech., Mach., Robot. Mechatron. Sci. 58, 115–125. doi:10.1007/978-3-319-89911-4_9.

Li, W., Chen, G., Yeo, S., 1999. Viscoelastic properties of MR fluids. J. Non Newton. Fluid Mech. 57 (1), 1–25.

Lifshitz, E.M., Kosevich, A.M., Pitaevskii, L.P., 1986. Chapter I – Fundamental equations. In: Grabbe, E., Ramo, S., Wooldridge, D. (Eds.), Theory of Elasticity. Butterworth-Heinemann, Oxford, UK, pp. 1–37.

Lord Corporation, 2017. MRF-132DG Magneto-Rheological Fluid Datasheet. Available at: https://www.lord.com/sites/default/files/Documents/TechnicalDataSheet/DS7015_MRF-132DGMRFluid.pdf (accessed on 11 December 2017).

Lord Corporation, 2019a. Tecnical Data for the RD-8040-1 Damper. Data supplied by the company on 2 October 2019.

Lord Corporation, 2019b. RD-8040-1 and RD-8041-1 Dampers Datasheet. Available at: http://www.lordmrstore.com/lord-mr-products/rd-8040-1-mr-damper-short-stroke (accessed on 02 October 2019).

Meng, W.J., Wu, S.M., Liu, B.L., et al., 2017. Multi-physics analysis of a magnetorheological brake with double coils placed on side housing. Key Eng. Mater. 739, 252–263 10.4028/www.scientific.net/KEM.739.252.

Metered, H., Bonello, P., Oyadiji, S.O., 2010. The experimental identification of magnetorheological dampers and evaluation of their controllers. Mech. Syst. Sig. Process. 24 (4), 976–994. doi:10.1016/j.ymssp.2009.09.005.

Meyers, M., Chawla, K., 2008. Mechanical Behavior of Materials. Cambridge University Press, UK.

Papanastasiou, T.C., 1987. Flows of materials with yield. J. Rheol. 31 (5), 385–404. doi:10.1122/1.549926.

Parlak, Z., Engin, T., 2012. Time-dependent CFD and quasi-static analysis of magnetorheological fluid dampers with experimental validation. Int. J. Mech. Sci. 64 (1), 22–31. doi:10.1016/j.ijmecsci.2012.08.006.

Parlak, Z., Engin, T., Çallı, İ., 2012. Optimal design of MR damper via finite element analyses of fluid dynamic and magnetic field. Mechatronics 22 (6), 890–903. doi:10.1016/j.mechatronics.2012.05.007.

Purandare, S., Zambare, H., Razban, A., 2019. Analysis of magnetic flux in magneto-rheological damper. J. Phys. Commun. 3 (7), 075012. doi:10.1088/2399-6528/ab33d7.

Purcell, E.M., Morin, D., 2013. Electricity and Magnetism, Third ed. Cambridge University Press, Cambridge, UK.

Sapiński, B., Jastrzębski, Ł., Gołdasz, J., 2020. Electrical harmonic oscillator with MR damper and energy harvester operating as TMD: experimental study. Mechatronics 66, 102324. doi:10.1016/j.mechatronics.2020.102324.

Seid, S., Chandramohan, S., Sujatha, S., 2018. Optimal design of an MR damper valve for prosthetic knee application. J. Mech. Sci. Technol. 32 (6), 2959–2965. doi:10.1007/s12206-018-0552-7.

Stanway, R., 2004. Smart fluids: current and future developments. Mater. Sci. Technol. 20 (8), 931–939. doi:10.1179/026708304225019867.

Susan-Resiga, D., 2009. A rheological model for magneto-rheological fluids. J. Intell. Mater. Syst. Struct. 20 (8), 1001–1010. doi:10.1177/1045389X08100979.

Syrakos, A., Dimakopoulos, Y., Tsamopoulos, J., 2018. Theoretical study of the flow in a fluid damper containing high viscosity silicone oil: effects of shear-thinning and viscoelasticity. Phys. Fluids 30 (3), 030708. doi:10.1063/1.5011755.

Wang, D.H., Bai, X.X., Liao, W.H., 2010. An integrated relative displacement self-sensing magnetorheological damper: prototyping and testing. Smart Mater. Struct. 19 (10), 105008. doi:10.1088/0964-1726/19/10/105008.

Wang, D.H., Liao, W.H., 2011. Magnetorheological fluid dampers: a review of parametric modelling. Smart Mater. Struct. 20 (2), 023001. doi:10.1088/0964-1726/20/2/023001.

Wang, Y., Li, S., Meng, W., 2017. Strong coupling analysis of fluid–solid for magnetorheological fluid braking system. J. Intell. Mater. Syst. Struct. 29 (8), 1586–1599. doi:10.1177/1045389X17742730.

Yu, J., Dong, X., Sun, S., et al., 2020. Comparison of dynamic models based on backbone curve for rotary magneto-rheological damper. Proc. Inst. Mech. Eng. Part C: J. Mech. Eng. Sci. 234 (14), 2732–2740. doi:10.1177/0954406219856392.

Yuan, X., Tian, T., Ling, H., et al., 2019. A review on structural development of magnetorheological fluid damper. Shock Vib. 2019, 33. doi:10.1155/2019/1498962.

Zhao, Y.-L., Xu, Z.-D., 2018. A hysteretic model considering Stribeck effect for small-scale magnetorheological damper. Smart Mater. Struct. 27 (6), 065021. doi:10.1088/1361-665x/aabc2c.

Zheng, J., Li, Z., Koo, J., et al., 2014. Magnetic circuit design and multiphysics analysis of a novel MR damper for applications under high velocity. Adv. Mech. Eng. 6, 402501. doi:10.1155/2014/402501.